Simulating satellite urban land surface temperatures: sensitivity to sensor view angle and assumed landscape complexity

Remote Sensing of Environment 293 (2023) 113579

Contents lists available at ScienceDirect

Remote Sensing of Environment

journal homepage: www.elsevier.com/locate/rse

Simulating satellite urban land surface temperatures: sensitivity to sensor view angle and assumed landscape complexity

William Morrison [a,*], Sue Grimmond [a], Simone Kotthaus [a,b]

[a] Department of Meteorology, University of Reading, Earley Gate, Reading RG6 6BB, UK
[b] Institut Pierre Simon Laplace (IPSL), CNRS, École Polytechnique, Institut Polytechnique de Paris, 91128 Palaiseau Cedex, France

ARTICLE INFO

Edited by Dr. Marie Weiss

Keywords:
Obstacle resolving modelling
Radiation modelling
LST
Urban
DART
Satellite LST

ABSTRACT

Urban land surface temperature (LST) from satellite earth observation (EO) varies with sensor view angle. Where these variations are not accounted for, urban LST products are inconsistent through time, limiting their use in urban weather and climate model evaluations and process studies (e.g. urban heat island, building energy balance, human thermal comfort). Obstacle-resolving numerical models (ORM) of urban form and radiation exchanges are being used to: (a) understand relations between EO view angle, the 3-dimensional urban surface, and the surface temperatures from urban land surface models, and (b) evaluate parameterisations (parametric models) that aim to account for LST angular effects for the next operational satellite products. Most ORM are limited to simplified buildings (e.g. cuboids) and surface temperatures by lack of datasets. Novelly, we use both a realistic urban form model and observed surface temperatures to assess the impact of simplifying the urban form and temperature on the modelled LST anisotropy. We test various sets of assumptions in central London by combining ground-based thermal camera observations and the state-of-the-art Discrete Anisotropic Radiative Transfer (DART) model. The high resolution realistic model (< 1 m) includes thermal (surface temperatures varying by sun-surface geometry, shadow history and materials every 30 min) and geometry (sloped roofs, chimneys and vegetation) data. These data are used to simulate brightness temperatures of EO pixels to quantify LST view angle variations.

During daytime, a change of view angle of 47° off-nadir corresponds to a difference in LST of up to 5.1 K for the realistic building model. The intermediate-complexity landscape (easily obtainable building geometry/footprints and more idealised surface temperature distributions driven only by shadow patterns) gives the best agreement in simulated LST to the realistic landscape. The directional variations are still captured in total (daytime mean absolute error 0.44 K) when using an idealised ORM representation of the same landscape (cuboid buildings, simplified surface temperature) except for roofs which are near-isotropic. Results suggest that geometry assumptions used in current ORM are suited for evaluation of parametric models used to develop and verify operational LST sensor view angle corrections. Future work should consider more realistic materials and scattering processes including low emissivity glass and metals with challenging specular properties.

1. Introduction

Surface temperature is a central variable in the surface energy balance. Satellite-derived land surface temperature (LST) can provide a spatially continuous, global product that has been used to map surface urban heat islands (Yang H et al., 2020; Miles and Esau, 2020) and urban air temperature (Venter et al., 2020) for an improved understanding of the effects of cities on the climate and heat stress of populations. Urban land surface models increasingly use LST for model evaluation (Giannaros et al., 2013; Hu et al., 2014). However, any remote sensing (RS) observation is limited to a two-dimensional view of the surface-leaving radiance to determine LST (Jiang et al., 2018). Urban three-dimensional (3D) morphology and complex surface materials create directionally variable (i.e. anisotropic) surface-leaving radiance (Krayenhoff and Voogt, 2016). Surface-leaving radiance sampled by a remote sensor can therefore change depending on the view angle. For example, an observation viewing directly downward (i.e. nadir) is biased towards the surface-leaving radiance from horizontal surfaces (Roth et al., 1989; Voogt and Oke, 1997; Hu and Wendel, 2019), missing the large wall area contributing to the "complete" surface temperature across all surfaces (Jiang et al., 2018; Yang J et al., 2020). Anisotropy of surface-leaving

* Corresponding author.
E-mail addresses: william.morrison@meteo.uni-freiburg.de (W. Morrison), c.s.grimmond@reading.ac.uk (S. Grimmond).

https://doi.org/10.1016/j.rse.2023.113579
Received 26 September 2022; Received in revised form 7 April 2023; Accepted 10 April 2023
Available online 10 May 2023

Abbreviations

Symbol/ acronym	Description [unit]
3DM	Three-dimensional model
DART	Discrete Anisotropic Radiative Transfer model
EO	Earth observation
i	Surface component index
ILU	3D T_s distribution using DART solar illumination approach
Λ	Maximum T_b^{EO} difference between two view angles [K]
L_A	Leaf area density
LOD	Level of detail
LST	Nonspecific land surface temperature
M21	3D T_s distribution using (Morrison et al., 2021) approach
MAE	Mean absolute error
MBE	Mean bias error
ORM	Obstacle resolving model
PAI	Plan area index
PM	Parametric model
P_n	n^{th} percentile
T_b	Brightness temperature [K]
T_b^{EO}	Earth observation directional brightness temperature [K]
T_s	Skin surface temperature [K]
x, y	Image pixel coordinates
ΔT_b^{EO}	Off-nadir - nadir T_b^{EO} difference [K]
θ	Azimuth angle [°]
ϕ	Zenith angle [°]

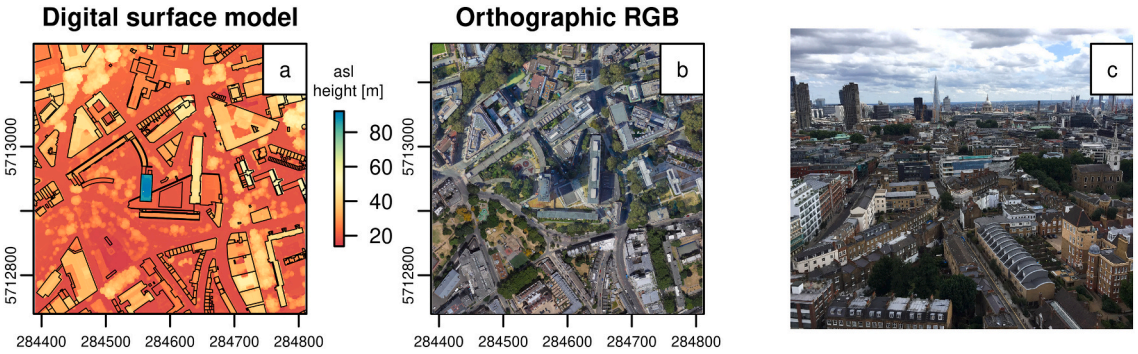

Fig. 1. Study area: (a) height of all surfaces above sea level (asl) from Google Earth imagery (Morrison et al., 2020) with building footprints (black lines, from Evans et al. (2011)), (b) orthorectified RGB image from a mosaic of Google Earth (Google, 2019) images (c) looking south east from 76 m roof centre of scene. Coordinate Reference System WGS84 UTM grid zone 31 N.

radiance across urban canopies is defined as an "effective" thermal anisotropy, to differentiate from the thermal anisotropy exhibited by individual surface components (Voogt and Oke, 1998a) caused by the non-Lambertian properties of real-world surfaces, including specular reflections from glass and metals. Effective thermal anisotropy in urban areas can give rise to directional variations in LST of over 10 K (Lagouarde et al., 2010) and is unaccounted for in current LST retrievals. This can confound estimates of surface urban heat island intensity through time and is considered a major source of model evaluation inconsistency between observed and modelled LST (Hu et al., 2014), along with cloud contamination. Further, it reduces LST climate record consistency, which is crucial if LST is to be considered a viable essential climate indicator or variable (WMO, 2016; ESA, 2019) or to be used routinely in data assimilation.

Future operational LST retrievals will convert angular LST to nadir or hemispherical temperature products by including models which normalise the angular variations (Cao et al., 2019) or "complete" surface temperature weighted across the full urban envelope (Voogt and Oke, 1997; Jiang et al., 2018; Yang J et al., 2020). The proposed models are semi-empirical parametric models (PM) that are computationally efficient and do not rely on complex inputs of land surface type, structure or component temperature distribution (Cao et al., 2019). PM describe the underlying processes of angular LST using kernels for (e.g.) emissivity, sun angle and shadow distributions. These are analytically expressed using multi-angular LST datasets, e.g. overlapping GOES-E and GOES-W measurements (Vinnikov et al., 2012) or combined geostationary and polar orbiters (e.g. Jiménez et al., 2012). Recently proposed PMs consider urban building/road geometry (Wang et al., 2020) and urban vegetation geometry (Cao et al., 2021; Jiang et al., 2021).

Using concurrent multi-angle LST for implementation of PM presents challenges. Observations from different satellites have spatial and temporal mismatches and have systematic product/instrumentation uncertainties (Ermida et al., 2014). Only ASTR and SLSTR sensors operate with two observation angles (Liu et al., 2020). Even differences in capture time for a multi-angle and multi-instrument observations (e.g. ~10 min) can have an effect as urban facets exhibit large fluctuations in surface temperature at short time scales (Christen et al., 2012). Quantifying these uncertainties requires detailed evaluation from high-resolution observations and simulations.

3D models (hereafter "3DM") or obstacle resolving models (ORM) offer a detailed, physical basis to evaluate PMs and multi-angle LST through explicit definition of the observed surface geometry and temperature distribution. However, available ORM approaches also vary in terms of building complexity and representation of real-world surface temperature variability. For example, Jiang et al. (2018) evaluate the PM of Vinnikov et al. (2012) and simulate scenarios when multi-angular LST were unavailable using an ORM (CoMSTIR) with idealised surface temperatures and cuboid buildings. Wang et al. (2020) evaluated the GUTA PM using the DART ORM (Wang et al., 2018) configured with repeating idealised buildings. It is the overarching objective of this study to quantify the implications of assumptions during the ORM setup. This is vital so that ORM can then be used to assess uncertainties inherent in PM used to support the next generation of LST retrievals.

ORM require a 3D description of the surface of interest to determine upwelling radiance (e.g. DART – Discrete Anisotropic Radiative Transfer, Gastellu-Etchegorry et al. (2015)), surface temperature fields (e.g. TUF-3D – Temperature of Urban Facets, Krayenhoff and Voogt (2007)) or to interpret sensor view (e.g. SUM - Surface-sensor-sun Urban Model, (Soux et al., 2004)). The idealised geometries greatly simplify model setup and input parameters. Improving geometry and surface

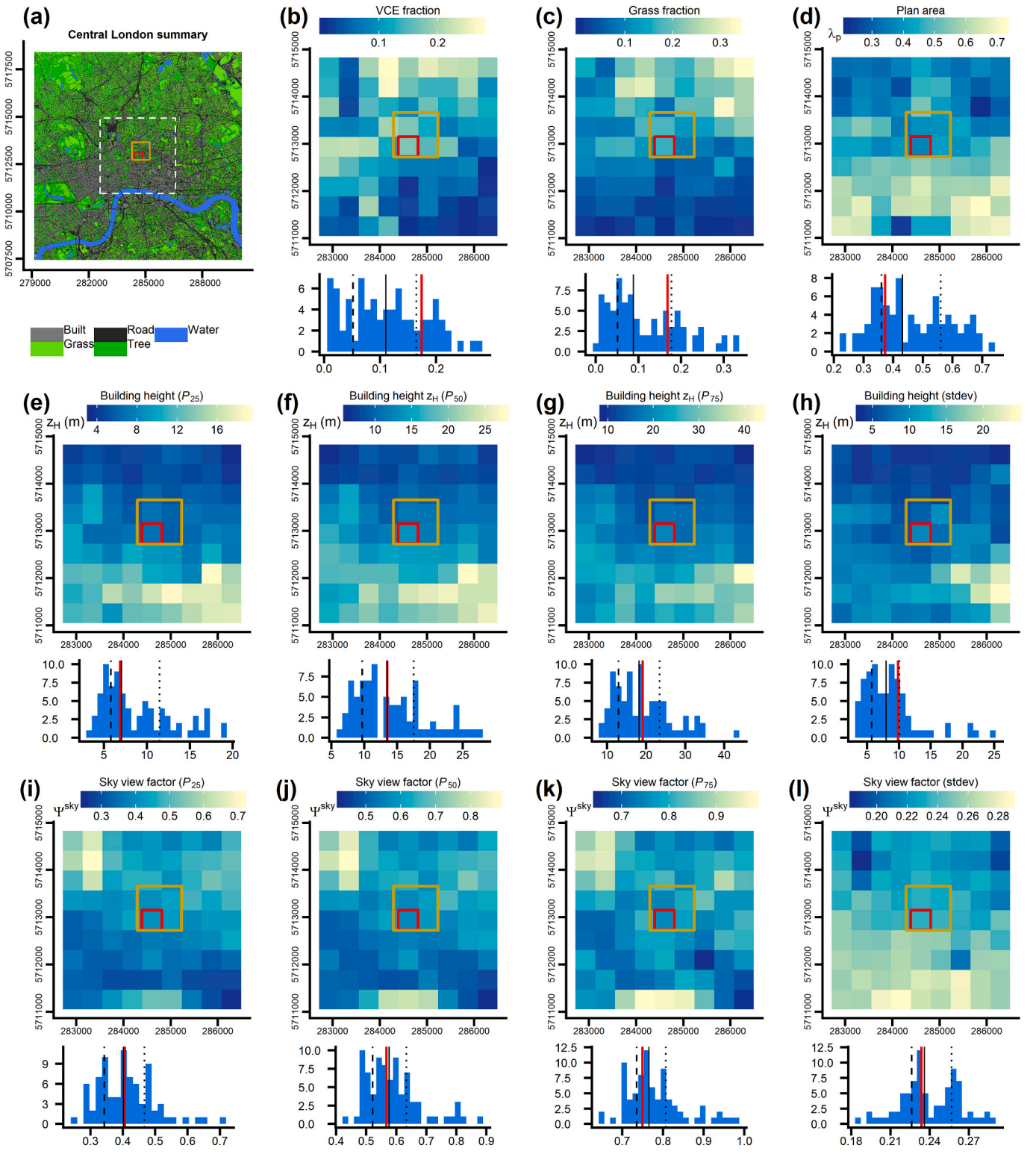

Fig. 2. Variability of surface characteristics in central London between grid-cells ($n = 81$, each 420 m × 420 m) compared to the study area (red) with (upper) maps and (lower) histograms with nth percentiles (P_n) of $P_{25} \rightarrow P_{75}$ (dashed lines), P_{50} (solid line), with solid red line the study area value. (a) Land cover (4 m resolution) with extent of maps (white dashed box) in b – l and a sample MODIS M*D11A1 pixel (orange box). Surface characteristics: (b) plan area fraction of tall vegetation (> 2 m) (c) plan area fraction of grass (d) plan area fraction of buildings (i.e. plan area index), (e – h) building height, (i – l) sky view factor (Dozier and Frew, 2002) calculated in R (R Core Team, 2017) with the "horizon" package (Van Doninck, 2018), and (g, l) standard deviation of the respective parameter. Maps oriented to grid north (WGS84 UTM grid zone 31 N). (For interpretation of the references to colour in this figure legend, the reader is referred to the web version of this article.)

Table 1
Study area (Fig. 1a, 420 x 420 m) land cover fractions and variability of heights (Morrison et al., 2020) and sky view factor (Gál and Unger, 2014; Dorman, 2021).

	Trees & Shrubs	Building	Grass
Plan area fraction	0.17	0.37	0.17
Percentiles	Height (m)	Height (m)	Sky view factor
P25	6.82	6.9	0.41
P50	10.01	13.49	0.57
P75	15.21	19.1	0.75

temperature characterisation requires rarely available detailed datasets (Masson et al., 2020) or more complex model design (i.e. beyond frequently used plane-parallel building grids such as in TUF-3D; ENVI-met, Gál and Kántor (2020)).

A range of urban characteristics have not yet been addressed by previous thermal anisotropy modelling applications:

i. With cuboid buildings and flat surfaces, sub-facet scale (e.g. < 1 m) *shadowing* is not accounted for. Sub-facet shadows can reduce a wall's mean surface temperature by 1–7 K (Hilland and Voogt, 2020), whereas roof shape (pitch and structure) can cause variations of over 20 K (Morrison et al., 2021). Prior ORM studies of LST anisotropy without micro-scale 3D structure hence tend to underestimate the anisotropy (Lagouarde et al., 2010; Krayenhoff and Voogt, 2016).
ii. *Urban vegetation* is often a large fraction of the urban surface (Small and Lu, 2006) and generally much cooler than impervious surfaces (Meier and Scherer, 2012). To our knowledge only Dyce and Voogt (2018) have used ORM with urban vegetation to simulate directional LST, but using plane-parallel building and vegetation canopies (see i.).
iii. *Surface temperatures* from ORM are very sensitive to model parameters that describe the surface composition (e.g. material thickness, heat capacity, albedo, emissivity). Still, to date neither these parameters nor the ORM surface temperatures are extensively evaluated as the necessary observations are both challenging to obtain and have limited spatial and temporal footprints (Pigeon et al., 2008). Ground-based observations, such as those across a residential area (Adderley et al., 2015), an idealised scale model (Morrison et al., 2018) or the New York city skyline (Ghandehari et al., 2018), do not cover the full complexity and diversity of realistic urban geometries. Although airborne observations (e.g. Sugawara and Takamura, 2006; Lagouarde and Irvine, 2008) and vehicle transects (Voogt and Oke, 1998a) have greater spatial extent, and hence represent higher complexities, they are snapshots in time.
iv. *Urban materials* are generally unknown at high spatial (facet scale), spectral (short and longwave) and angular (e.g. specular reflectivity) resolution. Thus, ORM are typically prescribed with bulk and Lambertian optical properties. In stark contrast, real urban areas have extremely complex material distributions and spectral responses (Kotthaus et al., 2014), with plastic signatures (Guo and Li, 2020) and specularly reflecting glass and metal claddings (Kotthaus et al., 2014). "Cool" LST islands detected around tall buildings (Agathangelidis et al., 2020) may hence be anomalies associated with LST retrieval uncertainties caused by the influence of specific materials (e.g. high glass fraction) on the anisotropy (Crawford et al., 2018).

To assess such sources uncertainty in common ORM configurations and to quantify the relative impact of simplifying the urban form and temperature, respectively, this study uses a uniquely detailed model accounting for those characteristics (i.-iv.) commonly simplified elsewhere. This allows us to model urban thermal anisotropy, with varying degrees of complexity in the underlying processes whereby the implications of various assumptions can be quantified. Realistic urban form and surface temperatures that are neither often nor easily available are combined to simulate a heterogeneous urban area. The micro-scale surface structure of 3D buildings is here resolved to individual pitched roofs, chimneys, balconies. Building facets, ground surfaces and vegetation are assigned component surface temperatures derived from high-resolution thermal infrared camera observations. Using a state-of-the-art radiative transfer model, a "realistic baseline" simulation of urban anisotropy is performed that then serves as a refence to asses simplified model setups. The complex landscape is incrementally simplified to obtain descriptions similar to previous studies to and the ability to characterize angular LST variability is compared to the "realistic

Table 2
Central London study area is represented as three-dimensional model landscapes with variations in: surface geometry level of detail (LOD), surface temperature distribution (T_s^{3D}) and vegetation leaf area density (LAD). Landscapes are implemented in the DART radiative transfer model to simulate directional land surface temperature.

Landscape feature	Code	Description	Basis
Surface geometry level of detail description (summary in Fig. 3)	LOD2	Realistic buildings (e.g. pitched roofs, chimneys) and vegetation >2 m tall	Most realistic geometry directly from Google Earth (Morrison et al., 2020), including sub-facet scale features
	LOD1	Extruded building footprints. Same vegetation as in LOD2	Most widely available and easy to use format for 3D building morphology.
	LOD0	Randomly oriented cuboid buildings. No trees.	Assumed in parametric models (e.g. GUTA) and a constraint in many common 3D models (e.g. TUF-3D's plane-parallel cubes)
Surface temperature distribution (T_s^{3D}) (details in Table 4)	M21	Ground-based observations (Morrison et al., 2021) stratified by sun-surface geometry, shadow history and high/low albedo	Most detailed description available from observed surface temperature variation (Morrison et al., 2021)
	ILU	Same as M21 but no shadow history	A simpler scheme accounting only for sun-surface geometry; used in other models (e.g. Wang et al., 2018)
Leaf area density of trees/shrubs uniformly applied to all vegetation	LAD0	No vegetation (trees/shrubs)	Typical assumed in other models (except Dyce and Voogt (2018))
	LAD0.15	Uniform LAD = 0.15 m^2 m^{-3}	(Krayenhoff et al., 2020) upper range
	LAD0.7	Uniform LAD = 0.7 m^2 m^{-3}	(Lalic and Mihailovic, 2004a) lower range; also near (Klingberg et al., 2017) ~ 0.6 lower range
	LAD1.6	Unform LAD = 1.6 m^2 m^{-3}	(Lalic and Mihailovic, 2004a) upper range; used in London, UK (Jeanjean et al., 2017); within (Klingberg et al., 2017) upper range (1.5–2)

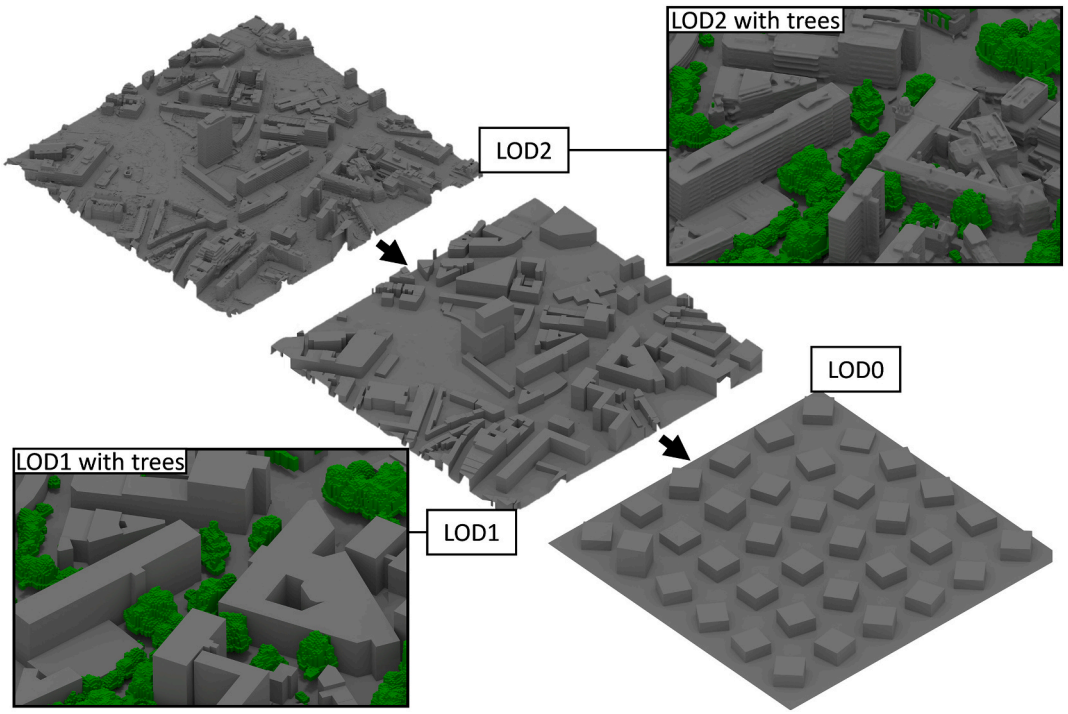

Fig. 3. Digital surface model (DSM) level of detail (LOD) variations in the model landscapes. Highest detail (LOD2) from Morrison et al. (2020) uses Google Earth Pro data (Google, 2019), simplified (LOD1) as extruded building footprints (Evans et al., 2011) and idealised (LOD0, schematic) using study area building height, number, and plan area (Table 1).

Table 3
Uncertainty range used in morphometric parameters for the lowest level of detail (LOD0) geometry description of the London study area. EO indicates earth observation techniques are used.

LOD0	Uncertainty	Details
Plan area index (PAI)	± 10%	> 90% accuracy [EO building masks in European cities] (Esch et al., 2020)
Mean building height	± 3 m	Mean bias error [EO in Germany] = 3 m (Frantz et al., 2021)
Building spacing	± 25%	Real-world cities have irregular building spacing (Chen et al., 2017)

baseline" to understand which details are most relevant for future comparisons to PM implemented in LST retrievals.

2. Methods

2.1. Modelling satellite LST variation by view angle

The Discrete Anisotropic Radiative Transfer (DART) model (Gastellu-Etchegorry et al., 2012) (Section 2.1.2) can simulate satellite-derived urban LST as brightness temperatures (T_b^{EO}) for different "landscapes" (Section 2.1.1). As DART can model T_b^{EO} for any zenith (ϕ) and azimuth (θ) view angles (°), this allows variations across different landscapes to be assessed. Taking nadir sampled temperatures [$T_b^{EO}(\phi = 0)$, i.e. "straight down" EO view] as reference, the difference (ΔT_b^{EO}) to off nadir [$T_b^{EO}(\phi, \theta)$] is:

$$\Delta T_b^{EO} = T_b^{EO}(\phi, \theta) - T_b^{EO}(\phi = 0) \quad (1)$$

The overall T_b^{EO} range (i.e. maximum (max) to minimum (min)) for distribution of temperatures at a given view angle is (Krayenhoff and Voogt, 2016):

$$\Lambda = max\left[T_b^{EO}(\phi, \theta)\right] - min\left[T_b^{EO}(\phi = 0)\right]. \quad (2)$$

2.1.1. Model landscape

In this study, the term "landscape" describes a 3D model of urban form and surface temperature. Here, the urban form includes the buildings, ground, and vegetation, overlaid with a 3D surface temperature field with 1 m × 1 m × 1 m resolution voxels (Appendix A). Each voxel holds a data point (here surface temperature) for a given volume. Landscapes are created (Section 2.3) and then implemented in DART (Section 2.1.2) to simulate T_b^{EO}.

2.1.2. DART radiative transfer model

DART (here version 5.7.5) is a computer model that simulates radiative transfer in heterogeneous 3D landscapes. Using a ray tracing approach, DART determines the emission and multiple scattering of individual longwave infrared (LWIR) rays across a landscape. The result can be a 2D image of a landscape's surface-leaving thermal radiance [L^{surf}(x, y, ϕ, θ, *i*, λ, Ω), W m^{-2} sr^{-1} μm^{-1}] across a horizontal plane at the top of the landscape (the bottom of atmosphere – BOA) (Yin et al., 2015; Wang and Gastellu-Etchegorry, 2020) at a given wavelength (λ, μm), with (x, y) the image pixel indexed by surface component(s) *i* (e.g. roof and/or wall), ϕ and θ (°) the zenith and azimuth propagation angles, and Ω (sr) the solid angle. Hereafter for brevity, Ω and λ are no longer stated explicitly as simulations are performed at a single selected wavelength and use uniform solid angle. For each timestep, 116 2D images are computed for directions θ = 0 → 360°. To reduce computation time, the number of image files, and the data stored, only images for φ < 50° are simulated.

To determine a landscape's view angle variation in upwelling radiance, L^{surf}(x, y, ϕ, θ, *i*) is resampled to obtain a landscape mean surface-leaving radiance typical for EO resolutions:

$$L^{surf}(\phi, \theta) = \frac{1}{n} \sum_{(x,y)}^{n} L^{surf}(x, y, \phi, \theta, i) \quad (3)$$

Table 4
Surface properties used to both stratify surface temperature observations and allocate them to a 3D landscape. Surface temperatures variation method M21 (Morrison et al., 2021) and ILU (Table 2). Acronyms see list at start of paper. Note as a BRF is relative to the illumination of a flat surface, a vertical surface (e.g. a wall) facing the sun is illuminated more than the reference flat surface, hence a BRF ratio is >1.

Surface property name	Obtained in 3D using	Surface property description	Surface property stratification		Used in
Orientation and material	Blender (Blender, 2018) 3D modelling, airborne hyperspectral data (Morrison et al., 2020)	Cardinal facing wall orientation. Boolean high/low albedo roof separation for LOD2 geometry (constant low albedo for LOD1 and LOD0)	Roof (low albedo) Roof (high albedo) Ground (impervious) Ground (grass) North facing East facing	South facing West facing Down facing	M21, ILU
Sun-surface geometry	DART shortwave simulation	Bidirectional reflectance factor (BRF)	Lambertian BRF: 0 (shaded) → 2 (most sunlit) [Δ0.25 steps] (unitless)		M21, ILU: boolean sun or shade
Shadow history	DART shortwave simulation shadow tracking through time (Morrison et al., 2021).	Recently shaded surfaces cool exponentially with time constant (τ, min); maximum interval 2τ (or until ambient temperature reached)	2τ Roof = 86 min (fastest cooling) 2τ Ground = 269 min 2τ Walls = 347 min (slowest cooling) (Morrison et al., 2021)		M21

with n the number of image pixels. $L^{\mathrm{surf}}(\phi, \theta)$ then relates to $T_{\mathrm{b}}^{\mathrm{EO}}(\phi, \theta)$ by inversion of the Planck function (B_{λ}^{-1}) at the simulation wavelength (λ, μm):

$$T_{\mathrm{b}}^{\mathrm{EO}}(\phi, \theta) = B_{\lambda}^{-1}\left[L^{\mathrm{surf}}(\phi, \theta)\right]. \quad (4)$$

Here $\lambda = 11.02$ μm is used, corresponding to the centre of MODIS (Moderate Resolution Imaging Spectroradiometer) band 31. A split window (Zhengming Wan and Dozier, 1996) or other (e.g. Islam et al., 2017) LST retrieval would then use L^{surf} at different bands and consider neither the view angle or facet (i) level radiative exchange processes.

2.1.3. DART vs. previous sensor view modelling of anisotropy

Previous sensor view modelling of thermal anisotropy to derive $T_{\mathrm{b}}^{\mathrm{EO}}(\phi, \theta)$ has determined the weighted contribution from various surface types (e.g. sunlit/shaded wall, roof, ground) for different view angles (e.g. Lagouarde et al., 2010):

$$T_{\mathrm{b}}^{\mathrm{EO}}(\phi, \theta)^4 = \sum_{i}^{n_i} f_i(\phi, \theta)\left(T_{\mathrm{b},i}\right)^4 \quad (5)$$

where $f_i(\phi, \theta)$ is the view fraction of surface component i within the sensor field of view determined by a sensor view model (e.g. Soux et al., 2004), $T_{\mathrm{b},i}$ is the surface component brightness temperature from observations or energy balance modelling, and n_i is the total number of surface components. Surface components act independently and are typically opaque; but have included tree crowns (Dyce and Voogt, 2018).

DART surface components can instead have radiative contributions from anisotropic scattering, transmission through turbid media (e.g. vegetation) and the (cloud-free) sky and are not constrained to idealised geometry (cuboid buildings, plane-parallel surfaces, smooth facets, etc.), bulk facet-level surface temperatures, or Lambertian emission.

2.2. Study area and observation period

The central London (UK) 420 m × 420 m study area has a mix of vegetation, high- and low-rise structures (Fig. 1). The analysis uses ground-based surface temperature observations taken in the area (Morrison et al., 2020; Morrison et al., 2021) for a mainly clear-sky summer day (27th August 2017).

To assess how representative the study area is of central London and a single EO pixel (e.g. MODIS/Sentinel) at a resolution of ~1 km × 1 km, the morphometric and land cover characteristics are analysed for a ~ 4 km × 4 km area around the site (Fig. 2a). South and east of the site is the central business district. Both average building height and plan area index (PAI, fractional area covered with buildings) decrease northwards, while vegetation fraction increases in more residential areas. The study area PAI is similar to the surroundings (Fig. 2), but there is more vegetation (> 75th percentile of the extended area, Table 1 cf. Fig. 2b, c) associated with a park (Fig. 1b, centred at grid coordinates 284,500, 5,712,850).

As earlier ground-based thermography studies were undertaken in less built-up areas, our site's median building height (13.5 m, Table 1) is greater than both (Adderley et al., 2015) area-weighted building height of 6.23 m and (Morrison et al., 2018) 1.5 m cubes. From visual inspection, the vegetation fraction is lower than in the (Meier and Scherer, 2012) study area.

2.3. Model landscapes of the study area

The study area surface geometry, vegetation and temperature are simulated to create a series of model landscapes (Table 2, more details in Appendix A). Digital surface models (DSM) are used to represent the 3D geometry of each landscape. Their resemblance to the "real world" are indicated by their level of detail (LOD), where LOD2 (Fig. 3) has the most realistic building features (e.g. sloped roofs, chimneys, and balconies) and LOD0 the most idealised. In LOD1, the building footprints Evans et al. (2011), Fig. 1a) are vertically extruded (using "3Dfier", (Commandeur, 2020) to create 3D buildings with flat roofs and walls. As building footprints are widely available (e.g. Microsoft's Open Street Map (Heris et al., 2020)) LOD1 models are relatively easy to produce and hence most commonly used.

In LOD0 (Fig. 3), cuboid buildings are used with random orientations constrained so each wall angle has the same weight in an effective thermal anisotropy (Wang et al., 2018) estimate. The baseline LOD0 has regularly spaced cubes of randomly assigned heights (informed by the LOD2's building height inter quartile range) with both the PAI and number of buildings from the LOD1 building footprint. As LOD0 requires the least input information and pre-processing, it could potentially parameterise urban geometry globally; although coarsely and less accurately than higher LOD datasets. A range of LOD0 geometries are derived (hereafter "LOD0 ensemble") to account for uncertainties in the

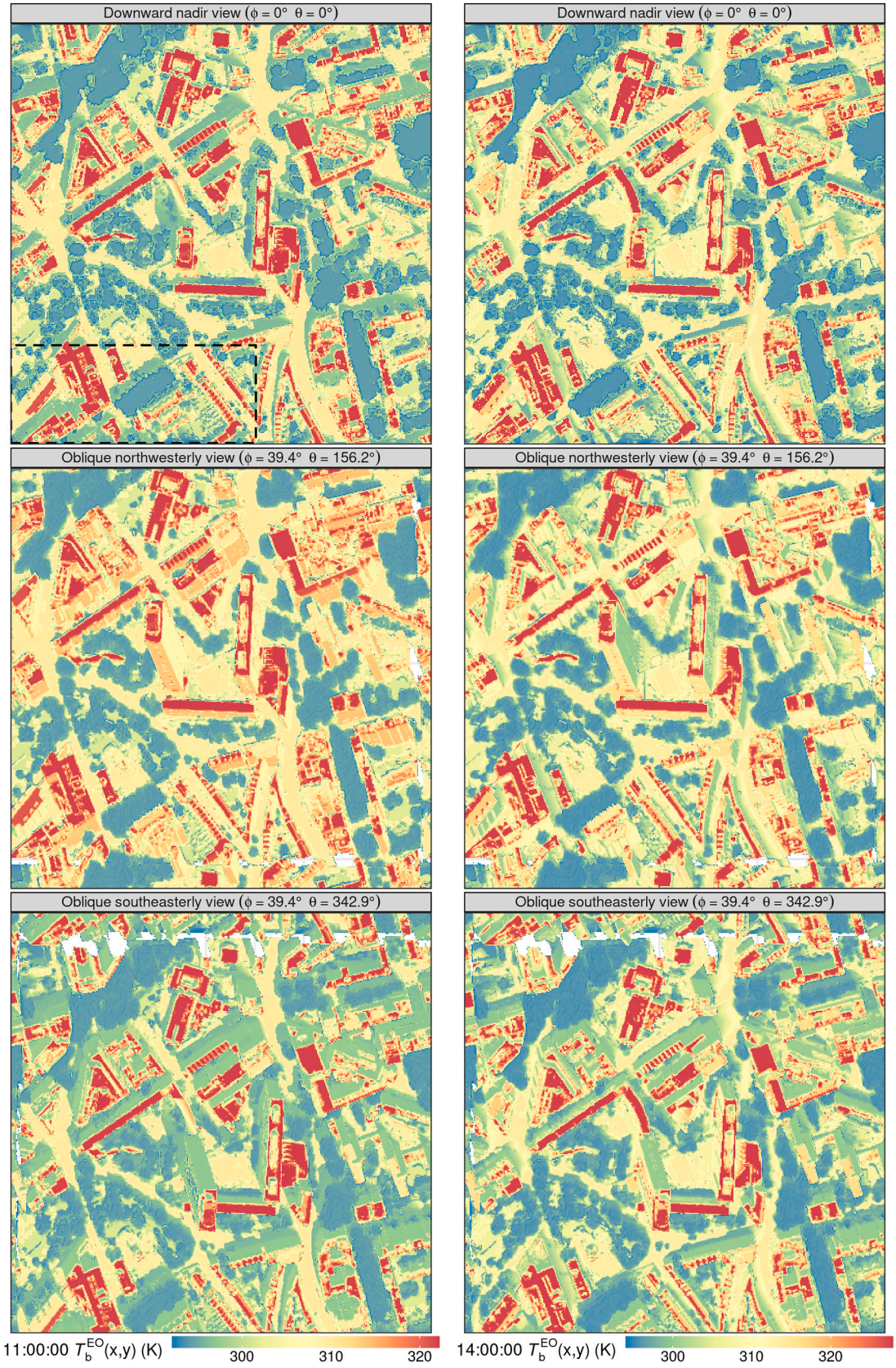

Fig. 4. Study area surface-leaving radiance shown as brightness temperatures (T_b) simulated using three-dimensional (3D) surface temperature derived from observations and the DART model for 27th August 2017 at (left) 11:00 and (right) 14:00 for (top) nadir and (middle – bottom) off-nadir zenith (ϕ) angles. Black dashed box (top left) is the area shown in Fig. 6a-d. Images have orthographic sensor perspective projection with surface → sky view directions such that: $\theta = 0^\circ$ is grid north and $\theta = 90^\circ$ grid east (WGS84 UTM grid zone 31 N) and $\phi = 0^\circ$ ($\phi = 90^\circ$) is viewing directly upward from (parallel to) the surface. White areas are the view inside buildings at the edge of the domain and masked from subsequent analysis.

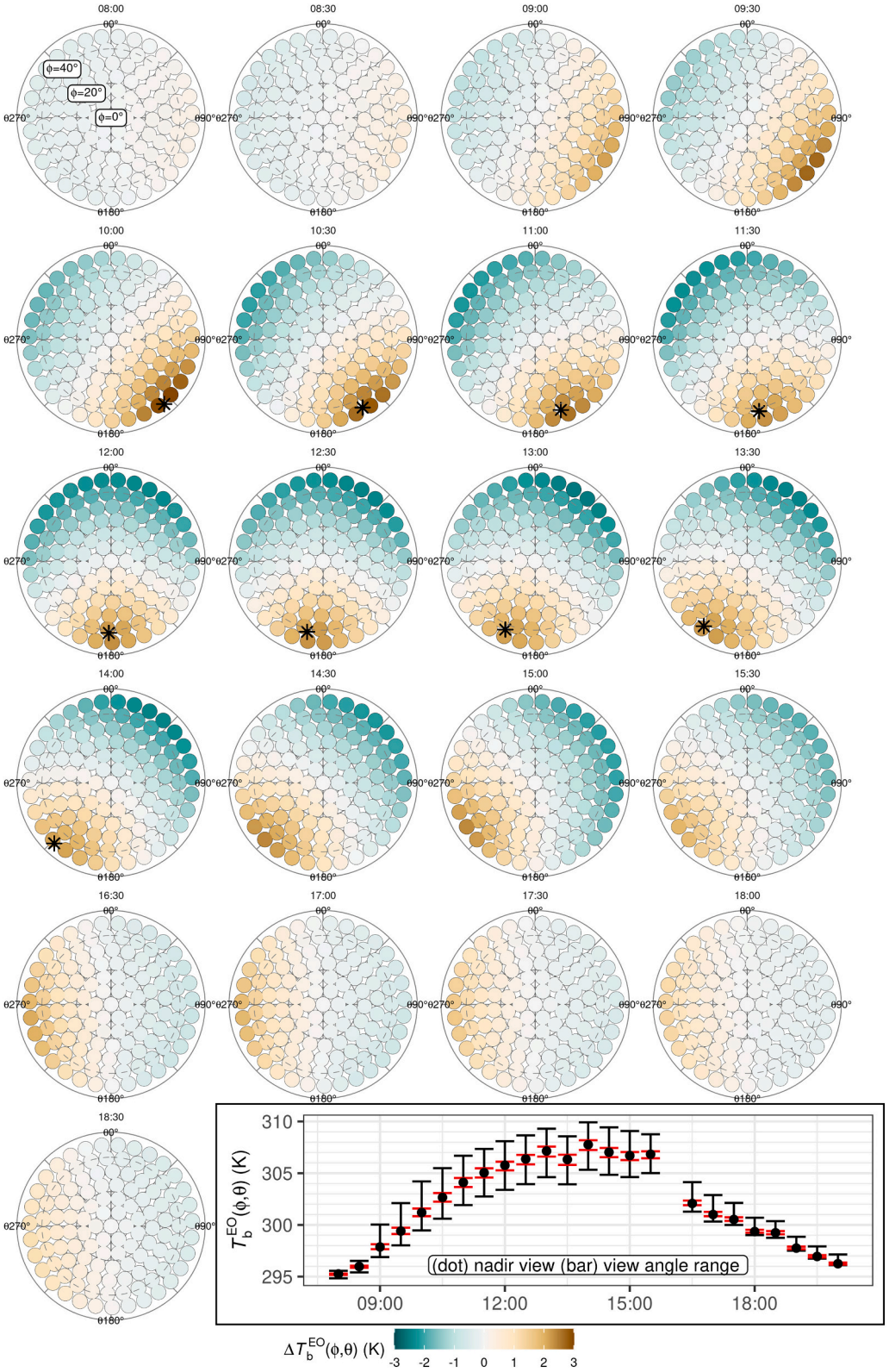

Fig. 5. Simulated thermal anisotropy for the study area with (polar plots) the difference in brightness temperature [$\Delta T_b^{EO}(\phi, \theta)$] from nadir temperature ($T_b^{EO}(\phi, \theta)$ - $T_b^{EO}(\phi = 0°)$) with zenith angle (ϕ, dashed lines with intervals top left plot) ≤ 47° simulated using observationally derived "M21" three-dimensional (3D) T_s (Morrison et al., 2021) across LOD2 geometry (same as Fig. 4) (Table 4). DART is used to simulate surface-leaving radiance for discrete directions (coloured dots). ϕ = 0° is radiation propagating upward and perpendicular to flat ground; ϕ = 90° is propagation parallel to flat ground; θ = 0° is radiation propagating true north and θ > 90° is radiation propagating eastward (etc.). Absolute simulated values (inset) show (dot) nadir T_b ($T_b^{EO}(\phi = 0°)$), (black bar) the T_b^{EO} range across any direction up to 47°off-nadir, and (red bar) the range for near-nadir (e.g. Landsat) views (ϕ < 8.8° $T_b^{EO}(\phi, \theta)$). (For interpretation of the references to colour in this figure legend, the reader is referred to the web version of this article.)

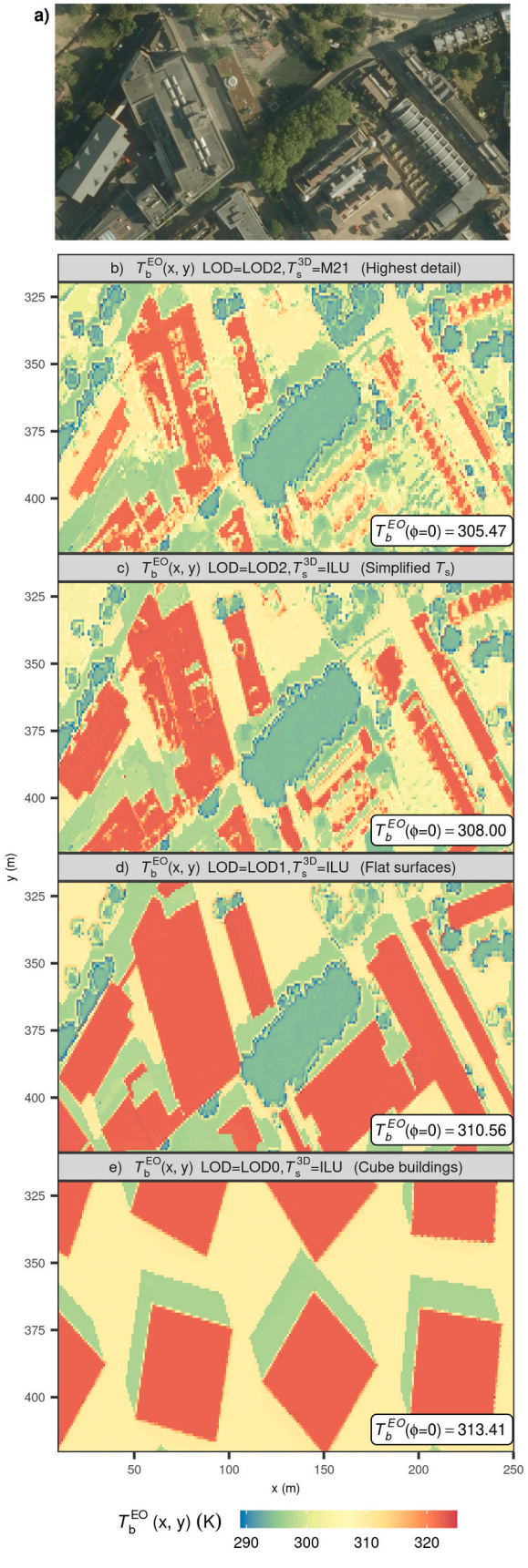

(caption on next column)

Fig. 6. Detail of Fig. 4 (black dashed lines): (a) aerial RGB image with similar shadow patterns (EDINA Digimap, 2015), (b-e) simulated high-resolution nadir-view (i.e. zenith angle $\phi = 0°$) images to represent earth observation (EO) products (x, y, pixels; m) of brightness temperature (T_b^{EO}(x, y)) using DART across landscapes with varied descriptions of surface geometry level of detail (LOD; LOD2 highest, LOD0 lowest) and three-dimensional surface temperature (T_s^{3D}), where M21 is complex (T_s^{3D} = M21) (Morrison et al., 2021) and ILU is simplified (T_s^{3D}=ILU). Labels (T_b^{EO} ($\phi = 0°$)) are image averages (with Planck function).

bulk parameters used (Table 3): PAI ±10% (Esch et al., 2020), building height ± 3 m (Frantz et al., 2021) and spacing of cubes randomly up to 25% from the regular spacing distance.

All DSMs are given a broadband emissivity of 0.93 based on observed mean impervious material values (Kotthaus et al., 2014). This is used by DART to simulate multiple scattering of longwave ($\lambda = 11.02$ μm, Section 2.1.2) radiation between surface components.

The vegetation in LOD1 and LOD2 are both the same, whereas for LOD0 there is no vegetation (Fig. 3). The vegetation is based on location of tall vegetation (i.e., non-grass) which includes trees and shrubs (> 2 m above ground level), hereafter *vegetation canopy elements* (VCE, Appendix A). As the leaf area density (LAD) can vary with vegetation type and volume, we consider some different densities (Table 2) but for each case all VCE voxels are assumed to have the same characteristics. The 1 m^3 voxels are assumed to be turbid with a spherical angular distribution of leaves, constant LAD and "deciduous leaf" optical properties at 11 μm from the DART spectral database (leaf transmissivity = 0.0145, reflectance = 0.0195).

2.4. Model surface temperature

Ground-based observations on a mostly cloud-free day at 30 min resolution are used to capture spatial and temporal variations of T_s that are known to vary over short distances (Lee et al., 2018; Aguerre et al, 2019; Morrison et al., 2021). Previous ground-truth of urban T_s are often limited to single-point infrared thermometers (e.g. Mathew et al., 2018; Wang et al., 2018), whereas we use thermal infrared cameras to better resolve spatial variations in surface temperature (Christen et al., 2012; Adderley et al., 2015). Observed surface temperatures (Morrison et al., 2021) are assigned to all landscape surfaces giving either a detailed distribution ("M21", Table 2), or simply based on solar illumination ("ILU", Table 2). The observed surface temperatures are corrected for atmospheric emission and absorption, and surface reflections, with uncertainties as determined by Morrison et al. (2020). Each voxel (X = Y = Z = 1 m) is assigned one T_s (T_s^{3D}(X, Y, Z)) in both methods (Appendix B). However, a voxel can contain more than one surface component; for example, a building corner may have both east and south facing walls, or a balcony a south, down and roof facing surfaces. In these cases T_s^{3D}(X, Y, Z, *i*) is set to the mean $T_s(i)$ of all surface components involved. The surface temperature voxels are saved as a pre-processing product for input into DART, with the surface temperature distribution across the DSM triangles determined by the triangle-cell intersection.

For M21, the thermal camera observations are stratified based on three surface properties *i* ($T_s(i)$) (Table 4) that drive surface temperature variation in urban areas (Morrison et al., 2021). These include: for example, a pitched roof's T_s can vary with orientation to the sun; materials with higher albedos are associated with lower surface temperature through the lower absorption of solar radiation; and the effects of thermal inertia (Aguerre et al., 2019) are stratified by a combination of facet type and time in shade rather than using overall aggregates (e.g. Voogt and Oke, 1998b; Morrison et al., 2018). For ILU, $T_s(i)$ is stratified using sunshine status, surface orientation, and material only (i.e. no shadow history, Table 4).

Following the GUTA PM (Wang et al., 2018) evaluation using DART, a surface component T_s range is calculated for direct input to the model. The range of mean temperatures is defined by shaded ("lower") and

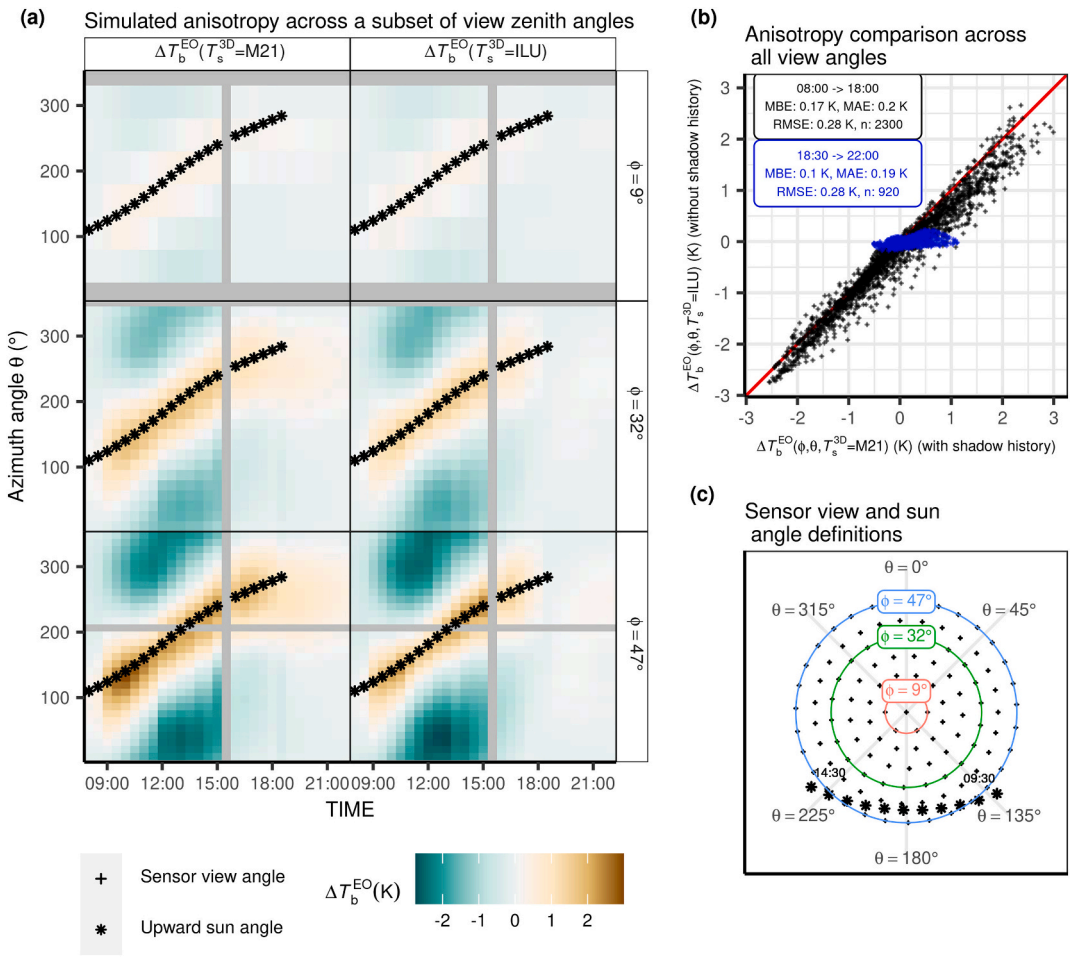

Fig. 7. Simulated satellite brightness temperature (T_b^{EO}) using DART and daytime ground-based observations across zenith view angles (ϕ) up to 47° off-nadir, shown as differences between nadir and off-nadir (ΔT_b^{EO}) for a central London study area using a realistic (LOD2, Fig. 3) landscape geometry and dense vegetation (LAD1.6, Table 2). ΔT_b^{EO} compared across two different three-dimensional (3D) surface temperature (T_s^{3D}) parameterisations derived from observations: T_s^{3D} = M21 varies by sun-surface geometry, facet type, shadow history, material. T_s^{3D}=ILU varies by sun/shade/facet type only. (b) ΔT_b^{EO} for (black) day (blue) night time off-nadir view angles for 08:00 → 22:00 27th August 2017 and (a) subset of view angles for (left) M21 and (right) ILU for all azimuth angles (θ, θ = 0° is UTM 31 N grid north, θ = 90° east, etc.) for (rows) three zenith view angles with (star) sun angle. Angle definitions (c) shows "upward" polar coordinate system used, i.e. angles measured with a ground to sky perspective, with (crosses) the discrete view angles, (coloured lines) the three zenith samples used in (a) and (stars) the 30 min upward sun angles from early morning (ϕ > 50°, θ < 135°) → midday (ϕ ≈ 40°, θ ≈ 180°) → late afternoon (ϕ > 50°, θ > 230°). (For interpretation of the references to colour in this figure legend, the reader is referred to the web version of this article.)

sunlit ("upper") limits. The "upper" limit T_s is prescribed in DART to any sunlit surface, and the "lower" T_s to any shaded surface. This gives 3D variations based on sun angle, DSM, and vegetation.

While M21 is the best estimate of a realistic T_s, ILU is both more easily simulated as it requires fewer surface temperature components, and more representative of studies limited by observations availability (e.g. IRTs, thermocouples, Li and Li (2020)) or idealised 3DM with plane-parallel geometry. The ILU setup is already implemented in DART, meaning the landscape geometry can change without needing to manually pre-process and store the M20 landscape temperature in large 5D numerical arrays (i.e., 3D space, shadow history timestep, surface class).

As the brightness temperature observations for vegetation are unstratified by sun-surface geometry, all VCE are assigned the same T_s. This is the observed air temperature measured 1 km south east of the study area (Morrison et al., 2020).

3. Results and discussion

First, the highest detail landscape simulation, informed by observations and 3D modelling, is analysed (Section 3.1). Based on this, the best estimate of 2D satellite observations are derived. The simulations are unprecedented both in terms of spatial resolution (< 1 m) and temporal continuity (30 min resolution for a day post-sunrise).

Second, this benchmark is used to study a comprehensive range of idealised landscapes (Section 3.2) based on similar assumptions used in previous simplified approaches to interpret effective thermal anisotropy. These simplified models are required to verify any future operational corrections (e.g. based on GUTA, Wang et al. (2020)) for effective thermal anisotropy.

3.1. Highest detail landscape simulation

3.1.1. Spatially resolved LST variations in response to satellite view angle

To quantify variations in LST in response to the view angle across, high spatial resolution directional brightness temperature images (T_b^{EO}(x, y, ϕ, θ)), a combination of LOD2 geometry and M21 surface temperature observations (Table 4) is used. Depending on the view angle, different surfaces are captured in the image (Fig. 4) which creates unique brightness temperature distributions. Roof, ground, and vegetation are viewed from the nadir direction. Off-nadir view angles also have wall surfaces visible, many with complex T_b distributions. The sub-

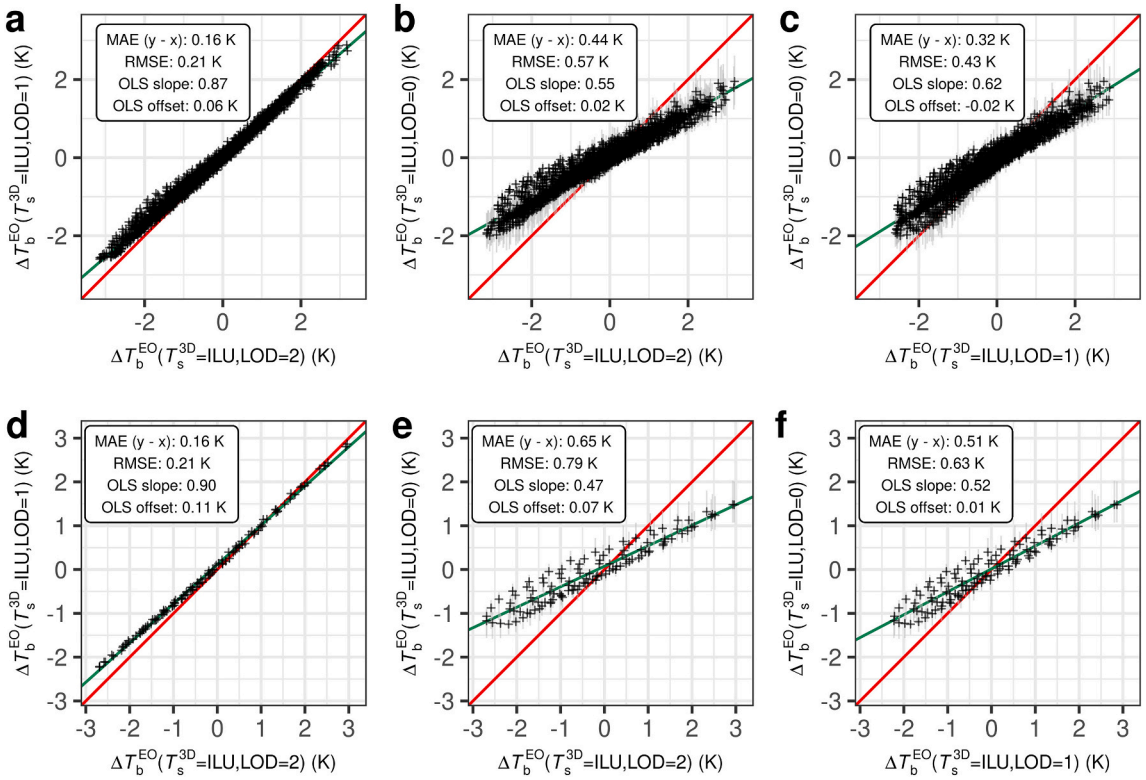

Fig. 8. Simulated satellite brightness temperature (T_b^{EO}) using DART and surface temperatures from daytime ground-based observations on 27th August 2017 (30 min intervals) for (a-c) 08:00 → 18:00 and (d-f) timestep with maximum anisotropy (10:30) across zenith view angles (ϕ) up to 47° off-nadir (any of a-c have n points = 4360), shown as differences between nadir (ϕ = 0°) and off-nadir (ΔT_b^{EO}) compared for landscapes with different building geometry level of detail (LOD) for a central London study area. All comparisons have no vegetation. 3D surface temperatures distributed by solar illumination (T_s^{3D}=ILU). (b, c) Error bars are the range from LOD0 ensemble simulations (±3 m building height, ±10% PAI, ±25% building separation, Table 3).

facet wall geometry creates contrasting temperatures around sunlit portions and cooler shaded areas (e.g. wall recesses, from balconies) or with oblique sun-surface angles. With simple planar surface geometry, wall T_b would vary only because of building shadows and/or shadow histories. The complex roof geometry creates similarly complex shadow patterns.

The colder vegetation creates T_b spatial patterns that contrast with warmer impervious surfaces. The generally homogeneous T_b (T_s prescribed based on air temperature, Section 2.4) is due to the uniform leaf area density (LAD0.7, Table 2).

3.1.2. *Temporally resolved thermal anisotropy*

While airborne studies capture temporal snapshots of anisotropy, here the analysis is continuous at 30 min resolution between 2 h after sunrise (08:00) and 2 h after sunset (22:00), allowing for a time series evolution of anisotropy (Fig. 5) to be investigated. It reveals that at 08:00, when T_s is similar between facet types (Appendix B), $T_b^{EO}(\phi, \theta)$ is near-isotropic across all view angles up to $\phi = 47°$ ($\Lambda = 0.7$ K, maximum anisotropy, Eq. 2).

$T_b^{EO}(\phi, \theta)$ is greater for off-nadir view angles around the sun angle (hot spots). At 10:00 $T_b^{EO}(\phi, \theta)$ peaks at 3.0 K warmer than nadir (301.2 K) ($\Lambda = 4.7$ K). Λ reaches 4.9 K at 10:30. The hot spot being found near the sun direction is consistent with prior mid-latitude observations (Hu and Wendel, 2019). The near-nadir (e.g. Landsat) views (here $\phi < 8.8°$, Fig. 5, red bars) have lower $T_b^{EO}(\phi, \theta)$ variation as expected ($\Lambda \leq 1.0$ K, $\Lambda = 1.0$ K at 12:30) with minimum 0.2 K at 08:00 and 20:00.

3.2. *Effect of landscape simplification on thermal anisotropy*

To identify key inter-landscape differences in brightness temperature from an earth observation perspective (T_b^{EO}) for the different landscape configurations (Fig. 3, Fig. 4) we discuss a subset (Fig. 6a) of the study area. The highest detail T_b^{EO} (LOD2 geometry and M21 T_s^{3D}, Fig. 6b) has the greatest $T_b^{EO}(x, y)$ variation (cf. Fig. 6c-e), particularly across roofs where sub-facet geometry (e.g. sloped roofs, chimneys) have diverse sun-surface geometries.

In Fig. 6b, M21's sun-surface geometry classification (BRF, Table 4) prescribes a range of T_s. For example, $T_b^{EO}(x, y)$ across the sunlit pitched roof (centred x = 25, y = 370) has around 307 K → 316 K $T_b^{EO}(x, y)$ difference between left (more east-facing) → right (more west-facing) sides. While the left side has a low sun illumination angle (low irradiance and BRF), the right side is almost perpendicular to the sun angle (high irradiance and BRF).

The parameterisation ILU (Fig. 6c) has Boolean "sunlit" and "shaded" temperatures across T_s^{3D} (Section 2.4). This results in the pitched roof being mostly homogeneous as it is prescribed "sunlit" roof T_s. Across other roofs, $T_b^{EO}(x, y)$ ILU varies only if there is self-shadowing from micro-scale roof features. ILU's lower micro-scale variation in roof temperature results in a $T_b^{EO}(\phi = 0°)$ (308.0 K) that is 2.5 K higher than for the M21 (305.5 K) case. Similar micro-scale effects have been reported for walls with ~20–40% self-shading (Hilland and Voogt, 2020).

With flat roofs (LOD1) there is no micro-scale T_s variation (Fig. 6d). LOD1's buildings are generally more pronounced given their flat facets with sharp right angles when roofs and walls intersect. Some buildings

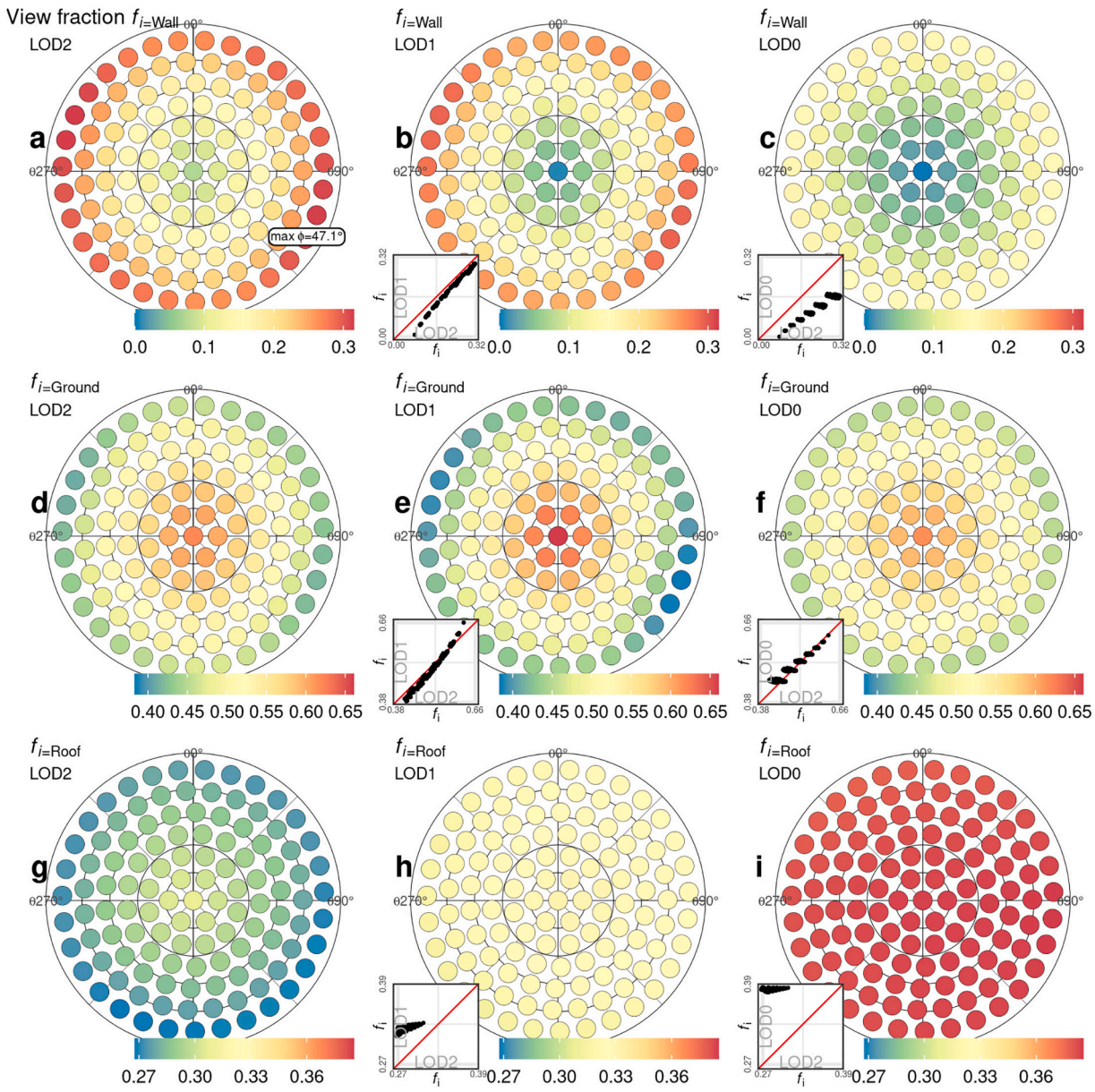

Fig. 9. View fraction *f* (Eq. C-4) of surface component (*i*) across simulated satellite perspective for (a-c) $f_{i=Wall}$, (d-f) $f_{i=Ground}$, and (g-i) $f_{i=Roof}$. Satellite perspectives simulated are for zenith angles (ϕ) 0° → 47° (central points are ϕ = 0°, black radial line grid spacing of 10°) and azimuth angles (θ) 0° → 360° with (colours, polar plots) the view fraction for a given direction. Scatterplots (insets) compare all directions between LOD2 (x-axis) and LOD*N* (y axis) with (red) 1:1 line. Landscapes based on different level of detail (LOD, see Fig. 3 for definitions): (a,d,g) LOD2 - most realistic urban geometry, (b,e,h) LOD1 – realistic building footprints, and (c,f,i) LOD0 idealised cube buildings. (For interpretation of the references to colour in this figure legend, the reader is referred to the web version of this article.)

are present in LOD1 but not in LOD2 (and vice versa) because of differing DSM data sources. LOD1, created around 2010, has buildings at x = 50, y = 390 and x = 0, y = 420 (Fig. 6) which are absent in LOD2 (created 2018). However, manual inspection across the study area, suggests the LOD1 footprints generally agree well with the LOD2 buildings (Fig. 1a).

For vegetation, both the geometry and temperature descriptions in the LOD1 and LOD2 simulations are the same. Hence, the VCE have homogeneous T_s. However near the canopy edges, T_b^{EO}(x, y) varies where the canopy is often thinner (e.g. Fig. 6b) allowing radiation from the warmer ground below to penetrate.

Although, the LOD0 cubes (Fig. 6e) have no micro-scale T_s variation and VCE are omitted, the T_s responds to the shadows cast on the ground creating the coolest regions. The cube roofs are warmest. The VCE are not included as the layout relative to real-world buildings (cf. cubes) is not matched. Using idealised cuboid vegetation to test the sensitivity of various vegetation and cube morphologies to thermal anisotropy (see Dyce and Voogt, 2018) is outside of this study's aims.

3.2.1. *Surface temperature distribution*

The two different surface temperature distributions (M20, ILU, Table 2, Table 4) are compared to understand the contribution of shadow history and surface cooling through time impact on T_b^{EO}(ϕ, θ) variations. T_b^{EO}(ϕ, θ) is simulated using the simplified temperature across the landscape (T_s^{3D}=ILU, Table 2) and compared to results using the complex distribution (T_s^{3D} = M21; Table 2, Section 3.1).

Across all off-nadir view angles through the day (08:00–22:00, Fig. 7b), the effective thermal anisotropy (defined here as the [off-nadir

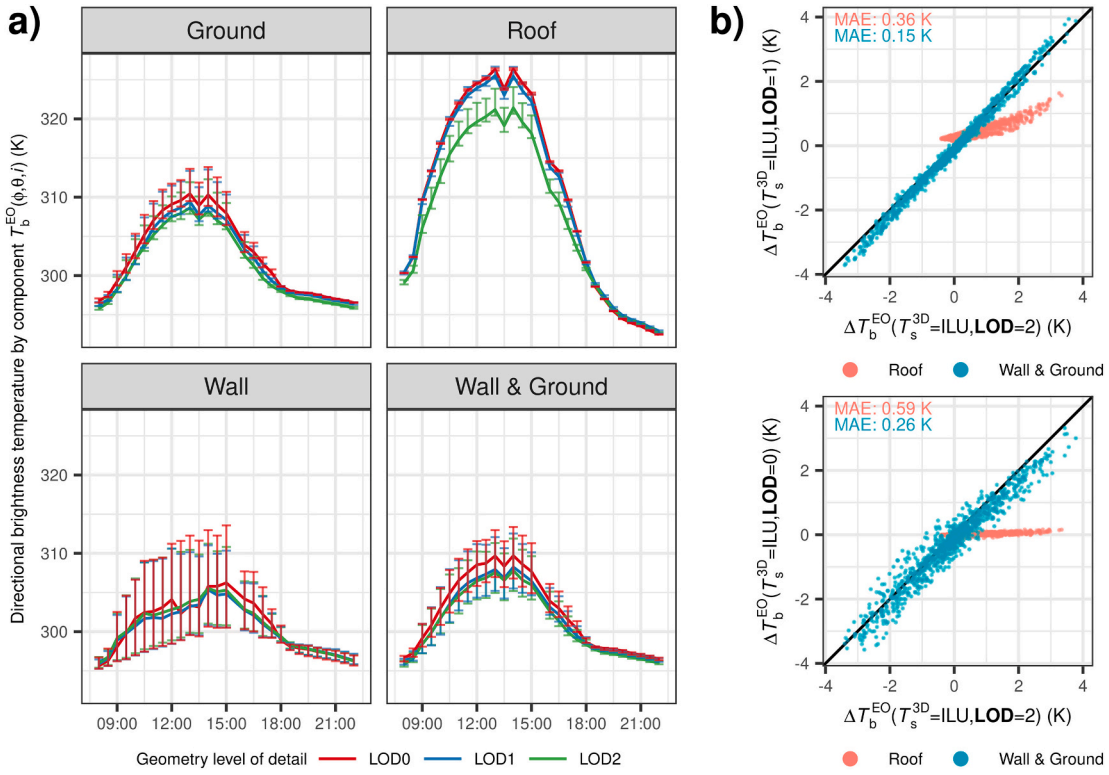

Fig. 10. Simulated satellite brightness temperature (T_b^{EO}) for different surface types i (e.g. i = Wall, i = Roof) for urban landscapes with different geometry level of detail (LOD) and surface temperatures (prescribed based on sun illumination, ILU) across view angles (ϕ, θ) up to 47° off-nadir showing (**a**) mean T_b^{EO}(ϕ, θ, i) and range (vertical lines) during the day (x-axis, UTC) for idealised cubes (LOD0) to realistic geometry (LOD2); and (**b**) contribution of surface components to anisotropy shown as [off nadir – nadir] differences ($\Delta T_b^{EO}(i)$ Eq. (1).

– nadir] difference, ΔT_b^{EO}; (Eqn 1) mean bias error (MBE) between ILU and M21 landscapes is 0.2 K, caused by variations around the sun angle hot spot. Analysis of thermal anisotropy through time (Fig. 7a) draws out the hot spot in relation to the sun angle. $\Delta T_b^{EO}(\phi, \theta, T_s^{3D} = \text{M21}) > 0$ K across a wider range around the sun angle for all timesteps.

As M21 resolves the thermal inertia with surface orientation (Supplementary Material, Appendix D), $\Delta T_b^{EO}(T_s^{3D} = \text{M21})$ can reproduce an observed asymmetrical hot spot (Lagouarde et al., 2010) caused by the "lags" of the azimuth hot spot behind the sun angle hotspot. After sunset (Fig. 7a, without *) $\Delta T_b^{EO}(T_s^{3D} = \text{M21})$ maintains a positive bias into the night, with a thermal inertia hot spot signal of $\Delta T_b^{EO} > 1$ K around θ = 200 → 300° until 21:30. In contrast, as T_s^{3D}=ILU has no thermal inertia, $\Delta T_b^{EO}(T_s^{3D}$=ILU) has no evening warm bias and has less variation (−0.5 → 0.5 K after sunset across all view angles). Across night-time intervals 18:30–22:00, the MAE is 0.19 K (Fig. 7b, blue).

3.2.2. *Surface geometry*

To isolate the importance of building shape complexity, the landscape DSM is simplified (LOD2 → LOD1 → LOD0) with one T_s^{3D} parameterisation (T_s^{3D}=ILU). Vegetation is excluded in LAD0 (Table 2). DART brightness temperatures are compared (ΔT_b^{EO}) between zenith view angles (ϕ) of up to 47° off-nadir and to nadir (ϕ = 0°).

Comparing across all 30 min time intervals (08:00–18:00) and ϕ settings, the anisotropy for the two lower LOD landscapes (Fig. 8 a-c, y axes) generally agrees well with LOD2. The planar facet geometry (ΔT_b^{EO}(LOD = 1)) agrees better with the LOD2 anisotropy (Fig. 8a, y axis) (MAE = 0.16 K) than the cuboid geometry (ΔT_b^{EO}(LOD0); MAE = 0.44 K; Fig. 8b). The linear regression (Fig. 8, green) slopes are lower for LOD0 (0.55) than LOD1 (0.87). Generally, a slope < 1 would indicate the more complex geometry (LOD2) is more anisotropic. The LOD2 ΔT_b^{EO} range is greatest (larger positive values) around the sun angle ("hot spot", Fig. 7) and has smaller negative values for azimuth angles 180° opposite the sun angle. Underestimation of anisotropy for LOD0 is consistent with prior low LOD modelling comparisons to observations (e.g. Krayenhoff and Voogt, 2016).

As anisotropy from surfaces' both view fractions (f_i(ϕ, θ), Appendix C) and temperatures ($T_{s,i}$, Eq. 5) drives ΔT_b^{EO}, these are explored to understand the differences in anisotropy in response to LOD (Fig. 8). LOD2 has the smallest roof view fraction ($f_{i=\text{roof}}$, Fig. 9g) as pitched roofs and awnings (etc.) with a deviation of >45° from horizontal are classified as a wall (Appendix A), with the lower roof fractions offset by higher fractions of wall. LOD2 $f_{i=\text{roof}}$ is the most anisotropic, decreasing from 0.31 at nadir to 0.27 for a view of south-facing surfaces (ϕ = 47.1°, θ = 214.1°; Fig. 9g). At nadir the tops of any convoluted roofs are most visible, but with increasing view angles lower roof structures can be occluded by other roof features. Comparing across all azimuth angles at ϕ = 47.1°, LOD2 $f_{i=\text{roof}}$ varies between 0.27 → 0.32.

LOD1 and LOD0 $f_{i=\text{roof}}$ are near-isotropic (~0.02 range, Fig. 9h, i), consistent with assumptions made in most parametric models and idealised 3DM. This makes $f_{i=\text{roof}}$ approximately same as the plan area index for any direction (Hu and Wendel, 2019; Wang and Chen, 2019). $f_{i=\text{ground}}$ is generally consistent across LODs (Fig. 9d-f).

T_s^{3D} varies between LODs even when using the same surface temperature distribution (T_s^{3D}=ILU), as differences in surface geometry translate into solar illumination patterns (e.g. through changes in sunlit and shaded fractions). To investigate these LOD effects, T_b^{EO}(ϕ, θ) is separated by component directional brightness temperatures (T_b^{EO}(ϕ, θ, i)). While T_b^{EO}(ϕ, θ) uses the radiance from all image pixels (Eq. 3, 4), T_b^{EO}(ϕ, θ, i) only uses the pixels that contain surface type i (Appendix C). T_b^{EO}(ϕ, θ, i) hence isolates the contribution of a given facet type to the variations in anisotropy.

LOD2 roof component brightness temperatures (T_b^{EO}(ϕ, θ, i = Roof))

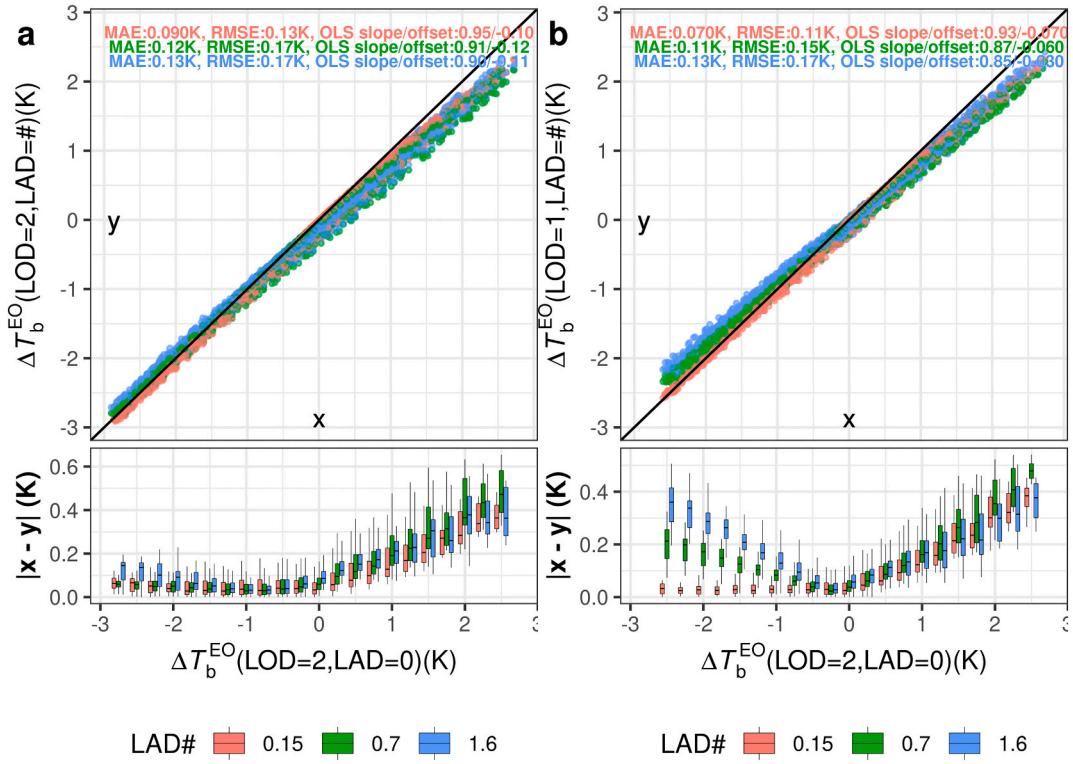

Fig. 11. DART simulated satellite brightness temperature (T_b^{EO}) for daytime (08:00 → 18:00 27th August 2017, 30 min intervals) ground-based observations across zenith view angles (ϕ) up to 47° off-nadir, shown as differences between nadir (ϕ = 0°) and off-nadir (ΔT_b^{EO}) compared for landscapes with varied geometry level of detail (LOD) and leaf area density (LAD) for a central London study area with (scatterplots, x-axis) a baseline ΔT_b^{EO} with no vegetation (LAD = 0, as Fig. 8c y axis) and high LOD geometry (LOD = 2, as Fig. 8a-b x-axis)) compared to (scatterplots, y axis, left) ΔT_b^{EO} with (colours) various LAD and (scatterplots, y axis, right) simplified LOD (LOD = 1, planar roofs and walls) with (bottom row) boxplots binned (0.25 K bins) across the baseline ΔT_b^{EO} showing absolute differences across the LAD and LOD variations. Boxplots show (box) inter-quartile range – IQR – (whiskers) 5 – 95th percentiles.

vary most with view angle (Fig. 10a, green vertical bars; Fig. 10b x-axes red points). Their pitched, micro-scale structure gives a range (Λ) of 0.6 K at 08:00, increasing to Λ = 2.3 K (09:00) with later maximum of Λ = 3.4 K (14:00). Whereas, LOD1 roofs maximum Λ is 1.5 K (14:00), while LOD0 roof Λ is always <0.3 K as there is no variation in the roof view fraction or surface temperature (i.e. $f_{i=\text{roof}}$, Fig. 9, or $T_b^{EO}(\phi, \theta, i = \text{Roof})$, Fig. 10a).

LOD2 roofs have a cool bias of over 5 K around midday. This is explained by high albedo "cool" surfaces (Appendix B, ~17.9% of total roof area, Morrison et al. (2021)) along with micro-scale geometry effects of self-shadowing, particularly from sloped surfaces towards/away from the sun (e.g. compare Fig. 6 b, d).

For wall and ground components, all LODs have directional brightness temperature variations (Fig. 10a) as for each view direction different shaded/sunlit fractions are seen. Brightness temperatures for LOD2 ground are lower – particularly at night – as LOD2 has a 0.17 grass fraction (Table 1) which has a relatively low surface temperature (Fig. B-1), whereas in the other LOD grass surfaces are unaccounted for. There is some unexplained azimuth variation in LOD1 wall and ground view fractions (Fig. 9b, e) perhaps from a bias in certain building orientations which, in central London, would be reduced when using a larger domain area containing more streets and buildings.

The combined anisotropy from walls and ground of LOD2 (Fig. 10b, blue) is similar to that of LOD1 and LOD0 ($MAE_{LOD1} = 0.15$, $MAE_{LOD0} = 0.26$ K) and thus contributes less to the overall inter-LOD ΔT_b^{EO} differences (Fig. 8). The generally high correlation between all landscapes (Fig. 8) is further understood through analysis of inter-landscape view fractions (Fig. 9) and facet temperatures (Fig. 10) which combined (e.g. Eq. (5) give rise to the observed anisotropy.

3.2.3. *Vegetation*

To investigate the impact of vegetation density on daytime anisotropy (Fig. 11) we compare a baseline ΔT_b^{EO} simulation with complex geometry but no vegetation ($\Delta T_b^{EO}(LOD = 2, LAD = 0)$) to cases with varying leaf area density (LAD). Generally, the baseline ΔT_b^{EO} has the most variation through time and with view angle.

Adding vegetation reduces the anisotropy (consistent with Dyce and Voogt (2018)) with greater reductions where $\Delta T_b^{EO} > 0$ K (Fig. 11, x-axes). For these viewing directions, the landscapes with LAD >0 have ΔT_b^{EO} around 0.4–0.6 K less than the baseline. Once vegetation is accounted for, there is little sensitivity to LAD (Fig. 11, colours) and LOD (Fig. 11, columns).

4. Conclusions

Urban geometry and surface temperature data are used to simulate directional variations of satellite brightness temperature images - the *effective thermal anisotropy*. Three-dimensional (3D) modelling of urban form and thermal radiative transfer processes using the Discrete Anisotropic Radiative Transfer (DART) model are used to explore the

relative importance of the geometry description, surface temperature representation and presence of vegetation. The study demonstrates these processes for a mainly clear-sky summer day in central London when high-resolution measurements were available.

For the first time, modelling of effective thermal anisotropy is not constrained to idealised descriptions of urban form and temperature. A realistic geometry with sub-facet features (e.g. pitched roofs and 3D vegetation canopies) is used as a reference standard to assess implications of using highly idealised urban geometry descriptions, such as repeating cube buildings, similar to what may be assumed in operational corrections of effective thermal anisotropy.

The 420 m × 420 m study area is similar to the larger central city surroundings (3 km × 3 km around the study area), based on morphometric parameters (e.g. building height, plan area) variability (defined here by interquartile range), except for tree cover (17%) that is within the 75th – 80th percentile. If similar detailed 3D model information and very high-resolution surface temperature data were available for a wider range of urban forms, the current simulations and analyses could be extended to capture a more representative diversity of intra- and inter-city variations in thermal anisotropy. However, such data do not yet exist for extensive areas.

Simulations of satellite, or Earth Observation (EO), views of the surface are used to quantify the effective anisotropy, defined as the difference in brightness temperature (T_b) between a view direction that is off-nadir (oblique) and a nadir (downward) view direction. The simulations use classified surface temperatures observations, whose allocation includes shadow state obtained from simulations considering either (1) known histories, or (2) instantaneous patterns. Although the anisotropy "hot spot" is generally broader if shadow history throughout the day is accounted for, both have close daytime agreement (MAE = 0.2 K). This allows the conclusion that instantaneous shadow patterns are a reasonable simplification when assigning surface temperatures in this urban setting in DART.

With instantaneous shadows as the basis to assign the facet temperature distributions, the role of the level of detail (LOD) of the building geometry on anisotropy is analysed based on three cases: realistic buildings (LOD2), planar roofs/walls (LOD1) and repeating cubes (LOD0). Consistent with earlier studies, anisotropy increases with increasing morphology detail. Simulated anisotropy using LOD1 is in closer agreement (daytime MAE = 0.16 K) to LOD2 than when using LOD0 (daytime MAE = 0.44 K).

The contribution of each facet type (roof, wall, ground) to the effective anisotropy is quantified for the three LOD. Changes in roof geometry complexity between LOD2 and LOD1 become apparent but in general both LOD lead to similar directional variations in the fraction of wall, roof and ground "seen" by the satellite (view fraction). LOD2 roof temperatures are generally cooler (on average 5 K cooler around midday) because of micro-scale shadowing. This micro-scale shadowing cool bias is the same order of magnitude as prior observational analysis. LOD2 results have more anisotropy than the flat LOD1 (and LOD0) roofs. Daytime directional brightness temperatures for the LOD2 roofs have a maximum 3.4 K range (14:00) compared to 1.5 K (0.2 K) for LOD1 (LOD0) (also at 14:00). The thermal anisotropy for the combined wall and ground facets are more consistent between LODs.

Including vegetation (trees, shrubs taller than 2 m) reduces the anisotropy for the daytime hot spot directions by around 0.4–0.6 K. Anisotropy is generally insensitive to variation in leaf area density, but future work should use the 3D radiative transfer modelling capabilities to investigate additional vegetation parameters (sunlit and shaded distributions, optical properties, leaf angular distributions, tree trunks and branches). Overall, vegetation is less important than LOD variation.

In this study, vegetation (median height = 10.01 m) is generally shorter than the buildings (median height = 13.49 m). Where vegetation frequently exceeds building heights (e.g. some residential settings) it may have greater implications on the effective thermal anisotropy because it would affect the roof fraction "seen" by the satellite.

Surface temperatures are prescribed based on several micrometeorological processes (solar illumination, shadow history, materials). Future studies should include broader spatial extents from airborne measurements that are spatially and temporally filled with facet-scale surface temperatures from energy balance models. Exploring the relative importance of geometry under different weather and climate conditions requires more observations. For example, the sensitivity of roof geometry to sun angle may differ during low winter sun angles.

This work has implications for how satellite based EO surface temperatures should be interpreted within urban areas and how EO data could be used in data assimilation and model evaluation in the future. Modelled thermal anisotropy using the easily derived LOD0 data are shown to give rapid and reasonable estimates compared to the more realistic cases. However, care should be taken using these lower LOD urban forms without prior evaluation at higher LOD. Expansion of the methods across different geometry and material emissivity configurations could test if the idealised LOD0 cases are applicable globally. There is scope for improving the material description of the realistic LOD2 cases, using increasingly available surface emissivity datasets through airborne and high-resolution satellite products. Implications of using idealised bulk emissivities can be explored, given highly reflective and specular surfaces common in cities (e.g. metals, glass) are expected to play a role in LST view angle sensitivity.

Declaration of Competing Interest

The authors declare that they have no known competing financial interests or personal relationships that could have appeared to influence the work reported in this paper.

Data availability

Data will be made available on request on zenodo.org (10.5281/zenodo.7896671).

Acknowledgements

This work is funded by EPSRC DARE (EP/P002331/1), MO Strategic Priorities Fund Climate Resilience Programme (IUS-UM100), H2020 UrbanFluxes (637519) and ERC urbisphere (855005). We thank Islington Council (Esther Lamontagne and Paul Stokes) for arranging access to observation sites and Kjell Zum Berge (University of Reading) for assistance with the observations.

Appendix A. Properties and description of the landscapes

To characterize the landscape opaque surfaces (e.g. buildings, roads) a vector-based 3D digital surface model (DSM) consisting of a 3D mesh of triangles is used. The vegetation canopy elements (VCE, any vegetation taller than 2 m) are a voxel array with $\Delta X = \Delta Y = 1$ m and $\Delta Z = 0.1$ m resolution.

The surface temperature and optical properties are resolved across voxels of uniform size in a 3D array at high resolution ($\Delta X = \Delta Y = \Delta Z = 1$ m). The spatial resolution of the landscape is the portion of digital surface model (DSM) triangles that occupies the volume of one surface voxel (a "surface element"). The voxel array stores the surface temperature distribution and a series of surface properties as a surface component (Table 4). Each surface element is assigned three properties: orientation and material (Σ), sun-surface geometry (bidirectional reflectance factor, BRF) and shadow history (time in shade, t_{shd}, (units = min)) which are all used to inform the upscaling of observed surface temperatures. The three properties combine to a unique surface component i at timestep t resulting in a 3D voxel array of surface components. By using surface elements, surface features such as geometry, material, optical and temperature properties can be determined at a flexible spatial resolution, instead of at the triangle scale of the DSM (e.g. radiosity models of Emig (2017); Ghandehari et al. (2018)); SOLENE model of Hénon et al. (2012)).

Optical properties at a wavelength of 11.02 μm are used, corresponding to the centre of MODIS (Moderate Resolution Imaging Spectroradiometer) band 31 (10.780–11.280 μm). For grass surfaces in LOD2 geometry, an emissivity based on the mean of all dry grass samples ($\varepsilon_{11.02\mu m} = 0.955$) in the MODIS UCSB (University of California, Santa Barbara) spectral library (Wan et al., 1994; Snyder et al., 1997) is used. As the surface material and associated emissivity are not well known for other DSM elements, the mean spectral emissivity ($\varepsilon_{11.02\mu m} = 0.93$; min = 0.900, max = 0.968, $n = 60$) from all non-metal and non-plastic impervious materials in the SLUM spectral library (Kotthaus et al., 2014) is used.

The vegetation optical properties are parameterised using a spatially homogeneous turbid representation of leaves with a spherical angular distribution (Wang et al., 2007; Pisek et al., 2011) within each vegetation voxel. Leaves are given "deciduous leaf" optical properties from the DART spectral database (leaf transmissivity = 0.0145, reflectance = 0.0195) with a leaf area density [leaf area within voxel / voxel volume ($m^2\ m^{-3}$)] (Lalic and Mihailovic, 2004; Jeanjean et al., 2017).

The downwelling longwave radiation across the landscape is assigned a predetermined isotropic source of downwelling spectral radiance received from a horizontal layer of the atmosphere that intersects the first vertical voxel layer above the landscape features (the bottom of atmosphere, BOA). The spectral radiance is determined from broadband longwave observations at the site (Morrison et al., 2020)

Appendix B. Landscape-wide M21 surface temperature

A surface temperature (T_s) of surface component i at timestep t [$T_s(i, t)$] is allocated to a 3D voxel array of surface temperature [$T_s(X, Y, Z, i, t)$]. An additional 3D voxel array that describes the surface components (i(X, Y, Z, t)) is used. Some surface component voxels can be ambiguous as they can contain DSM triangles with (e.g.) multiple surface orientations. For example, a voxel at the edge of a roof may contain a DSM triangle with both "roof" and "north" wall properties. In these cases, when determining $T_s(X, Y, Z, i, t)$, the mean temperature of all surface components involved is allocated.

B.1. Shadow history

The time series of binned bidirectional reflectance factor ($\overline{BRF}$) in three-dimensions ($\overline{BRF}(X, Y, Z, t)$) is used to estimate the time a surface element (Appendix A) has spent in shade (t_{shd}, min). $\overline{BRF}(X, Y, Z, t)$ is compared to the prior timestep [$\overline{BRF}(X, Y, Z, t - 5\ min)$]. If a surface element becomes shaded at time t, it has spent $t_{shd}(X, Y, Z, t) = 5$ min in shade. For the timestep prior to this (t – 5 min), the surface element has spent zero minutes in shade and has $t_{shd}(X, Y, Z, t - 5\ min) = 0$ min. A surface element that continues to be in shade [i.e. $\overline{BRF}(X, Y, Z, t + 5\ min) = -1$] has $t_{shd}(X, Y, Z, t + 5\ min) = 10$ min at the next timestep, etc.

A surface element can be part sunlit and part shaded, even across multiple timesteps. However, each voxel is reassigned as fully sunlit or fully shaded if appropriate based on a 50 min window around each timestep. Otherwise, if a surface element has $\overline{BRF}(X, Y, Z, t) > -1$, is sunlit at t – 25 min and shaded at t + 25 min, it is assumed the surface element could be partially sunlit. In these cases, the following threshold is used to determine if the surface element is more shaded than sunlit, and used to update t_{shd} by:

$$t_{shd}(X, Y, Z, t) = \begin{cases} 0 \text{ if } BRF(X, Y, Z, t) < [0.75 \cdot BRF(X, Y, Z, t - 25\ min)] \\ 5\ otherwise \end{cases} . \quad \text{(B-1)}$$

When $t_{shd}(X, Y, Z, t) = 0$, surface elements are allocated the maximum $\overline{BRF}(X, Y, Z)$ that occurred up to 5 timesteps prior (i.e. $\max\{\overline{BRF}(X, Y, Z, t - 25\ min \rightarrow 0)\}$) to assign partially shaded surfaces with a fully sunlit status.

Observations are aggregated based on their classification for the complete landscape surface to give a 3D surface temperature distribution [$T_s^{3D}(X, Y, Z, t)$]. The surface component i that combines the various surface properties (Table 4) use pixel-level thermal camera derived surface temperatures at timestep t ($T_s(x, y, i, t)$ (Morrison et al., 2021) aggregated to give temperatures stratified by surface component [$T_s(i, t)$] (Fig. B-1). Where a given surface component was not observed, $T_s(i, t)$ is gap-filled to ensure a temperature can be allocated to all surface elements.

Initial per-pixel surface temperature aggregation uses Σ and $\overline{BRF}$ for each timestep [$T_s(\Sigma, \overline{BRF}, t)$], excluding "mixed" and/or "masked" pixels. As there are more $T_s(\Sigma, \overline{BRF}, t_{shd}, t)$ combinations than observed, a shaded temperature [$T_s(\Sigma, \overline{BRF} = -1, t)$] is used.

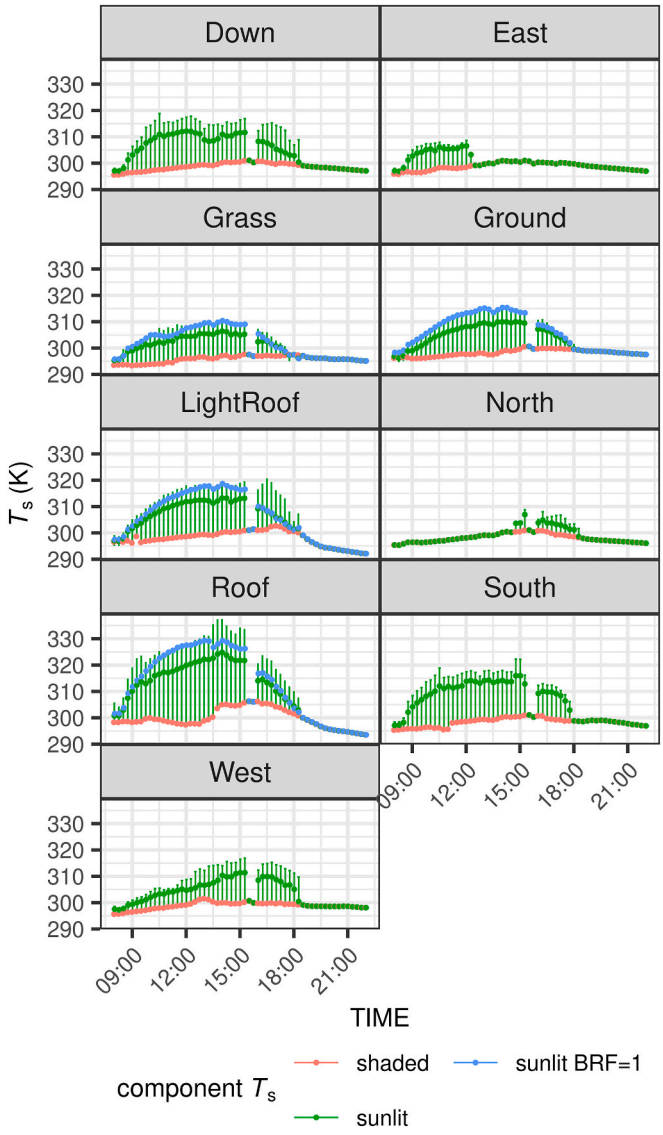

Fig. B-1. Surface component temperatures used as input for the three-dimensional surface temperature (T_s^{3D}) parameterisations with the range (vertical lines) of possible sunlit and recently shaded values that are used in the M21 parameterisation (Table 4), according to sun-surface geometry and time in shade and their mean (green points), with the ambient or "well shaded" surface temperature (red points) used in M21 and ILU and the ILU sunlit temperature (blue points) for bidirectional reflectance factor (BRF) of 1 (i.e. surface temperature representative of horizontal surfaces). (For interpretation of the references to colour in this figure legend, the reader is referred to the web version of this article.)

B.2. Gap-filling surface component temperatures

As observations do not cover all possible facets of the entire study area (i.e. more surface component permutations exist in 3D than are observed) gap-filling is required. With no downward facing surfaces (e.g. underside of balconies) sampled by any camera, 'all shaded walls' observations are used for this class of per-pixel gap-filling. Further gap-filling details of the observed surface temperature are given in (Morrison et al., 2021).

Appendix C. Calculation of surface component radiance and view fractions

The fraction of surface type i seen within an image (f_i) impacts directional variation in urban LST. If f_i for a nadir viewed urban surface has a plan area index of 0.5 (i.e. $f_{i=\text{Roof}} = 0.5$) and the remainder is ground, then $f_{i=\text{Ground}} = 0.5$, (i.e. all seen types equal 1). These values and components will change with view angle.

The simplest method to determine f_i for a given view angle ($f_i(\phi, \theta)$) is to sum the number of pixels per surface class i (e.g. $L^{\text{surf}}(x, y, \phi, \theta, i)$) and calculate a fraction relative to the total image pixels. However, this is inaccurate if an image pixel has surface-leaving radiance contributions from more than one surface component: the view fraction can be double-counted. Approaches to address this include: sensor view "sub-patches" (Krayenhoff and Voogt, 2016) assuming all components of a "mixed" pixel has the same temperature; and sensitivity tests to a "counted" f_i to the resolution of surface components derived from simulated RGB renders (Lagouarde et al., 2010).

Here we adopt a radiative transfer and energy conservation approach to calculation of f_i, using DART simulations. DART radiance images are calculated per surface component ($L_i^{\text{surf}}(x, y, \phi, \theta)$) and have surface-leaving radiance contribution after all scattering iterations. Whereas, L^{surf} (Eq. 3)

will always have the combined radiance contribution from all surface components. $L_i^{\text{surf}}(\phi, \theta)$ is related to $L^{\text{surf}}(\phi, \theta)$ by:

$$L_i^{\text{surf}}(\phi, \theta) = \frac{1}{n_{px}} \sum_{(x,y)}^{n_{\text{px}}} L_i^{\text{surf}}(\phi, \theta, x, y) \tag{C-1}$$

$$L^{\text{surf}}(\phi, \theta) = \sum_{i}^{n_{\text{img}}} L_i^{\text{surf}}(\phi, \theta) \tag{C-2}$$

i.e. the mean across all (n_{px}) L_i^{surf} image pixels is $L_i^{\text{surf}}(\phi, \theta)$ (Eq. C-1) and the sum of all (n_{img}) L_i^{surf} images is $L^{\text{surf}}(\phi, \theta)$ (Eq. C-2). L_i^{surf} pixels without surface component i have $L_i^{\text{surf}}(x, y, \phi, \theta) = 0$. L_i^{surf} pixels containing only a fraction of surface component i will have the associated fractional radiance contribution, which is more accurate than the aforementioned "simple approach" that resolves pixel-level view fractions.

A DART simulation for each landscape LOD is run in the thermal domain (11 μm) with a known isothermal temperature across all surfaces ($T_s^{3D} = 300$ K). All L_{surf} images have radiance $B^{-1}(300\text{ K}, \lambda = 11\ \mu\text{m}) = 9.57\ \text{W m}^{-2}\ \text{sr}^{-1}\ \mu\text{m}^{-1}$. With this total radiance contribution known and held constant, $L_i^{\text{surf}}(x, y)$ is then a fraction of $L^{\text{surf}}(x, y)$:

$$f_i(x, y, \phi, \theta) = L_i^{\text{surf}}(x, y, \phi, \theta) \Big/ \left(L^{\text{surf}}(x, y, \phi, \theta) = 9.57\right). \tag{C-3}$$

Across a whole image with n_{px} pixels, the view fraction of a surface component $f_i(\phi, \theta)$ is:

$$f_i(\phi, \theta) = \frac{1}{n_{\text{px}}} \sum_{(x,y)}^{n_{\text{px}}} f_i(x, y, \phi, \theta) \tag{C-4}$$

and the sum of n surface component fractions is unity:

$$\sum_{i}^{n} f_i(\phi, \theta) = 1 \tag{C-5}$$

The post-processing of these DART simulations is done in *R* using the daRt package (Morrison and Benjamin, 2020).

Appendix D. Satellite brightness temperature by surface component

The surface component directional brightness temperature $T_b^{EO}(\phi, \theta, i)$ considers the radiance contribution from image pixels of surface component i only. The DART radiance images $L^{\text{surf}}(x, y, \phi, \theta)$ are processed to have their pixels indexable by surface component i (Table 4) as $L^{\text{surf}}(x, y, \phi, \theta, i)$, which is first used to determine the image average radiance for a given surface component $L^{\text{surf}}(\phi, \theta, i)$:

$$L^{\text{surf}}(\phi, \theta, i) = \frac{1}{n} \sum_{(x,y)}^{n_{\text{px}}(i)} L^{\text{surf}}(x, y, \phi, \theta, i). \tag{D-1}$$

Here $n_{\text{px}}(i)$ is the number of pixels in the image that have a majority radiance contribution from surface component i ($f_i(x, y, \phi, \theta) > 0.5$, Eq. C-3). Finally, $T_{b,i}^{EO}(\phi, \theta)$ is calculated from the inverse Planck function of $L^{\text{surf}}(\phi, \theta, i)$ at the simulation wavelength (Eq. 6). Note: $L^{\text{surf}}(x, y, \phi, \theta, i)$ differs from $L_i^{\text{surf}}(x, y, \phi, \theta)$ (Appendix C).

Appendix E. Supplementary data

Supplementary data to this article can be found online at https://doi.org/10.1016/j.rse.2023.113579.

References

Adderley, C., Christen, A., Voogt, J.A., 2015. The effect of radiometer placement and view on inferred directional and hemispheric radiometric temperatures of an urban canopy. Atmos. Measur. Techn. 8 (7), 2699–2714. https://doi.org/10.5194/amt-8-2699-2015.

Agathangelidis, I., Cartalis, C., Santamouris, M., 2020. Urban Morphological Controls on Surface Thermal Dynamics : A Comparative Assessment of Major European Cities with a Focus on Athens, Greece.

Aguerre, J.P., et al., 2019. A street in perspective: thermography simulated by the finite element method. Build. Environ. 148, 225–239. https://doi.org/10.1016/j.buildenv.2018.11.007.

Blender, 2018. Blender 2.79b. Blender Institute, Amsterdam.

Cao, B., et al., 2019. A review of earth surface thermal radiation directionality observing and modeling: Historical development, current status and perspectives. Remote Sens. Environ. 232, 111304.

Cao, B., et al., 2021. A general framework of kernel-driven modeling in the thermal infrared domain. Remote Sens. Environ. 252, 112157 https://doi.org/10.1016/j.rse.2020.112157.

Chen, L., et al., 2017. The impacts of building height variations and building packing densities on flow adjustment and city breathability in idealized urban models. Build. Environ. 118, 344–361. https://doi.org/10.1016/j.buildenv.2017.03.042.

Christen, A., Meier, F., Scherer, D., 2012. High-frequency fluctuations of surface temperatures in an urban environment. Theor. Appl. Climatol. 108 (1–2), 301–324. https://doi.org/10.1007/s00704-011-0521-x.

Commandeur, T., 2020. tudelft3d/3dfier: version 1.3.0. Zenodo. https://doi.org/10.5281/zenodo.4280986.

Crawford, B., et al., 2018. Variability of urban surface temperatures and implications for aerodynamic energy exchange in unstable conditions. Q. J. R. Meteorol. Soc. 144 (715), 1719–1741. https://doi.org/10.1002/qj.3325.

Van Doninck, J., 2018. Horizon: Horizon Search Algorithm. Available at: https://cran.r-project.org/package=horizon. Available at:

Dorman, M., 2021. shadow: Geometric Shadow Calculations.

Dozier, J., Frew, J., 2002. Rapid calculation of terrain parameters for radiation modeling from digital elevation data. IEEE Trans. Geosci. Remote Sens. 28 (5), 963–969. https://doi.org/10.1109/36.58986.

Dyce, D.R., Voogt, J.A., 2018. The influence of tree crowns on urban thermal effective anisotropy. Urban Clim. 23, 91–113. https://doi.org/10.1016/j.uclim.2017.02.006.

EDINA Digimap, 2015. Aerial Imagery (25cm resolution), WMS web map service. Available at: https://digimap.edina.ac.uk.

Emig, T., 2017. Temperature distribution and heat radiation of patterned surfaces at short wavelengths. Phys. Rev. E 95 (5), 1–8. https://doi.org/10.1103/PhysRevE.95.052104.

Ermida, S.L., et al., 2014. Validation of remotely sensed surface temperature over an oak woodland landscape - the problem of viewing and illumination geometries. Remote Sens. Environ. 148, 16–27. https://doi.org/10.1016/j.rse.2014.03.016.
ESA, 2019. CCI Land Surface Temperature Algorithm Development Plan.
Esch, T., et al., 2020. Towards a large-scale 3D modeling of the built environment-joint analysis of tanDEM-X, sentinel-2 and open street map data. Remote Sens. 12 (15) https://doi.org/10.3390/RS12152391.
Evans, S., Hudson-Smith, A., Batty, M., 2011. 3-D GIS: Virtual London and beyond. https://doi.org/10.4000/cybergeo.2871. Cybergeo [Preprint].
Frantz, D., et al., 2021. National-scale mapping of building height using Sentinel-1 and Sentinel-2 time series. Remote Sens. Environ. 252 (June 2020), 112128 https://doi.org/10.1016/j.rse.2020.112128.
Gál, C.V., Kántor, N., 2020. Modeling mean radiant temperature in outdoor spaces, a comparative numerical simulation and validation study. Urban Clim. 32 (April 2019), 100571. https://doi.org/10.1016/j.uclim.2019.100571.
Gál, T., Unger, J., 2014. A new software tool for SVF calculations using building and tree-crown databases. Urban Clim. 10, 594–606. https://doi.org/10.1016/j.uclim.2014.05.004.
Gastellu-Etchegorry, J.P., et al., 2015. Discrete anisotropic radiative transfer (DART 5) for modeling airborne and satellite spectroradiometer and LIDAR acquisitions of natural and urban landscapes. Remote Sens. 7 (2), 1667–1701. https://doi.org/10.3390/rs70201667.
Gastellu-Etchegorry, J.P., Grau, E., Lauret, N., 2012. DART: A 3D model for remote sensing images and radiative budget of Earth surfaces. In: Modeling and Simulation in Engineering. InTech. https://doi.org/10.5772/31315.
Ghandehari, M., Emig, T., Aghamohamadnia, M., 2018. Surface temperatures in New York City: geospatial data enables the accurate prediction of radiative heat transfer. Sci. Rep. 8 (1), 1–10. https://doi.org/10.1038/s41598-018-19846-5.
Giannaros, T.M., et al., 2013. Numerical study of the urban heat island over Athens (Greece) with the WRF model. Atmos. Environ. 73, 103–111. https://doi.org/10.1016/j.atmosenv.2013.02.055.
Google, 2019. Google Earth Pro. Google [Preprint]. Google.
Guo, X., Li, P., 2020. Mapping plastic materials in an urban area: development of the normalized difference plastic index using WorldView-3 superspectral data. ISPRS J. Photogramm. Remote Sens. 169 (September), 214–226. https://doi.org/10.1016/j.isprsjprs.2020.09.009.
Hénon, A., et al., 2012. An urban neighborhood temperature and energy study from the CAPITOUL experiment with the solene model: part 2: influence of building surface heterogeneities. Theor. Appl. Climatol. 110 (1–2), 197–208. https://doi.org/10.1007/s00704-012-0616-z.
Heris, M.P., et al., 2020. A rasterized building footprint dataset for the United States. Sci. Data 7 (1), 207. https://doi.org/10.1038/s41597-020-0542-3.
Hilland, R.V.J., Voogt, J.A., 2020. The effect of sub-facet scale surface structure on wall brightness temperatures at multiple scales. Theor. Appl. Climatol. 140 (1–2), 767–785. https://doi.org/10.1007/s00704-020-03094-7.
Hu, L., et al., 2014. How can we use MODIS land surface temperature to validate long-term urban model simulations? J. Geophys. Res. 119 (6), 3185–3201. https://doi.org/10.1002/2013JD021101.
Hu, L., Wendel, J., 2019. Analysis of urban surface morphologic effects on diurnal thermal directional anisotropy. ISPRS J. Photogramm. Remote Sens. 148 (December 2018), 1–12. https://doi.org/10.1016/j.isprsjprs.2018.12.004.
Islam, T., et al., 2017. A physics-based algorithm for the simultaneous retrieval of land surface temperature and emissivity from VIIRS thermal infrared data. IEEE Trans. Geosci. Remote Sens. 55 (1), 563–576. https://doi.org/10.1109/TGRS.2016.2611566.
Jeanjean, A.P.R., et al., 2017. Air quality affected by trees in real street canyons: the case of marylebone neighbourhood in Central London. Urban Forest.Urban Green. 22, 41–53. https://doi.org/10.1016/j.ufug.2017.01.009.
Jiang, L., et al., 2018. Remote estimation of complete urban surface temperature using only directional radiometric temperatures. Build. Environ. 135 (March), 224–236. https://doi.org/10.1016/j.buildenv.2018.03.005.
Jiang, L., et al., 2021. Assessment of different kernel-driven models for daytime urban thermal radiation directionality simulation. Remote Sens. Environ. 263, 112562 https://doi.org/10.1016/j.rse.2021.112562.
Jiménez, C., et al., 2012. A comparison of ISCCP land surface temperature with other satellite and in situ observations. J. Geophys.Res.Atmos. 117 (8), 1–8. https://doi.org/10.1029/2011JD017058.
Klingberg, J., et al., 2017. Mapping leaf area of urban greenery using aerial LiDAR and ground-based measurements in Gothenburg, Sweden. Urban For. Urban Green. 26, 31–40. https://doi.org/10.1016/j.ufug.2017.05.011.
Kotthaus, S., Smith, T.E.L., Wooster, M.J., Grimmond, C.S.B., 2014. Derivation of an urban materials spectral library through emittance and reflectance spectroscopy. ISPRS J. Photogramm. Remote Sens. 94, 194–212. https://doi.org/10.1016/j.isprsjprs.2014.05.005.
Krayenhoff, E.S., et al., 2020. A multi-layer urban canopy meteorological model with trees (BEP-Tree): street tree impacts on pedestrian-level climate. Urban Clim. 32 (July 2019), 100590 https://doi.org/10.1016/j.uclim.2020.100590.
Krayenhoff, E., Voogt, J., 2016. Daytime thermal anisotropy of urban neighbourhoods: morphological causation. Remote Sens. 8 (2), 108. https://doi.org/10.3390/rs8020108.
Krayenhoff, S.E., Voogt, J.A., 2007. A microscale three-dimensional urban energy balance model for studying surface temperatures. Bound.-Layer Meteorol. 123 (3), 433–461. https://doi.org/10.1007/s10546-006-9153-6.
Lagouarde, J.P., et al., 2010. Modelling daytime thermal infrared directional anisotropy over Toulouse city centre. Remote Sens. Environ. 114 (1), 87–105. https://doi.org/10.1016/j.rse.2009.08.012.
Lagouarde, J.-P., Irvine, M., 2008. Directional anisotropy in thermal infrared measurements over Toulouse city centre during the CAPITOUL measurement campaigns: first results. Meteorog. Atmos. Phys. 102 (3–4), 173–185. https://doi.org/10.1007/s00703-008-0325-4.
Lalic, B., Mihailovic, D.T., 2004. An empirical relation describing leaf-area density inside the forest for environmental modeling. J. Appl. Meteorol. 43 (4), 641–645. https://doi.org/10.1175/1520-0450(2004)043<0641:aerdld>2.0.co;2.
Lee, S., et al., 2018. Analyzing thermal characteristics of urban streets using a thermal imaging camera: a case study on commercial streets in Seoul, Korea. Sustainability (Switzerland) 10 (2), 1–21. https://doi.org/10.3390/su10020519.
Li, N., Li, X., 2020. The impact of building thermal anisotropy on surface urban heat island intensity estimation: an observational case study in Beijing. IEEE Geosci. Remote Sens. Lett. 17 (12), 2030–2034. https://doi.org/10.1109/LGRS.2019.2962383.
Liu, X., et al., 2020. An improved method for separating soil and vegetation component temperatures based on diurnal temperature cycle model and spatial correlation. Remote Sens. Environ. 248 (July), 111979 https://doi.org/10.1016/j.rse.2020.111979.
Masson, V., et al., 2020. City-descriptive input data for urban climate models: model requirements, data sources and challenges. Urban Clim. 31 (August 2019), 100536 https://doi.org/10.1016/j.uclim.2019.100536.
Mathew, A., Khandelwal, S., Kaul, N., 2018. Analysis of diurnal surface temperature variations for the assessment of surface urban heat island effect over Indian cities. Energy Build. 159, 271–295. https://doi.org/10.1016/j.enbuild.2017.10.062.
Meier, F., Scherer, D., 2012. Spatial and temporal variability of urban tree canopy temperature during summer 2010 in Berlin, Germany. Theor. Appl. Climatol. 110 (3), 373–384. https://doi.org/10.1007/s00704-012-0631-0.
Miles, V., Esau, I., 2020. Surface urban heat islands in 57 cities across different climates in northern Fennoscandia. Urban Clim. 31 (August 2019), 100575 https://doi.org/10.1016/j.uclim.2019.100575.
Morrison, W., et al., 2018. A novel method to obtain three-dimensional urban surface temperature from ground-based thermography. Remote Sens. Environ. 215 (December 2017), 268–283. https://doi.org/10.1016/j.rse.2018.05.004.
Morrison, W., et al., 2020. Atmospheric and emissivity corrections for ground-based thermography using 3D radiative transfer modelling. Remote Sens. Environ. 237 (December 2019), 111524 https://doi.org/10.1016/j.rse.2019.111524.
Morrison, W., Kotthaus, S., Grimmond, S., 2021. Urban surface temperature observations from ground-based thermography: intra- and inter-facet variability. Urban Clim. 35, 100748 https://doi.org/10.1016/j.uclim.2020.100748.
Morrison, W., Benjamin, K., 2020. daRt: Read DART Model Outputs. https://github.com/willmorrison1/daRt.
Pigeon, G., et al., 2008. Simulation of fall and winter surface energy balance over a dense urban area using the TEB scheme. Meteorog. Atmos. Phys. 102 (3–4), 159–171. https://doi.org/10.1007/s00703-008-0320-9.
Pisek, J., Ryu, Y., Alikas, K., 2011. Estimating leaf inclination and G-function from leveled digital camera photography in broadleaf canopies. Trees - Struct.Funct. 25 (5), 919–924. https://doi.org/10.1007/s00468-011-0566-6.
R Core Team, 2017. R: A Language and Environment for Statistical Computing. Vienna, Austria.
Roth, M., Oke, T.R., Emery, W.J., 1989. Satellite-derived urban heat islands from three coastal cities and the utilization of such data in urban climatology. Int. J. Remote Sens. 10 (11), 1699–1720. https://doi.org/10.1080/01431168908904002.
Small, C., Lu, J.W.T., 2006. Estimation and vicarious validation of urban vegetation abundance by spectral mixture analysis. Remote Sens. Environ. 100 (4), 441–456. https://doi.org/10.1016/j.rse.2005.10.023.
Snyder, W.C., Wan, Z., Zhang, Y., 1997. In: Thermal Infrared bidirectional reflectance mea.pdf, 109, pp. 101–109 (July 1996).
Soux, A., Voogt, J.A., Oke, T.R., 2004. A model to calculate what a remote sensor "sees" of an urban surface. Bound.-Layer Meteorol. 112 (2), 109–132. https://doi.org/10.1023/B:BOUN.0000010995.62115.46.
Sugawara, H., Takamura, T., 2006. Longwave radiation flux from an urban canopy: evaluation via measurements of directional radiometric temperature. Remote Sens. Environ. 104 (2), 226–237. https://doi.org/10.1016/j.rse.2006.01.024.
Venter, Z.S., et al., 2020. Hyperlocal mapping of urban air temperature using remote sensing and crowdsourced weather data. Remote Sens. Environ. 242 (March), 111791 https://doi.org/10.1016/j.rse.2020.111791.
Vinnikov, K.Y., et al., 2012. Angular anisotropy of satellite observations of land surface temperature. Geophys. Res. Lett. 39 (23), 1–7. https://doi.org/10.1029/2012GL054059.
Voogt, J.A., Oke, T.R., 1997. Complete urban surface temperatures. J. Appl. Meteorol. 36 (9), 1117–1132. https://doi.org/10.1175/1520-0450(1997)036<1117:CUST>2.0.CO;2.
Voogt, J.A., Oke, T.R., 1998a. Effects of urban surface geometry on remotely-sensed surface temperature. Int. J. Remote Sens. 19 (5), 895–920. https://doi.org/10.1080/014311698215784.
Voogt, J.A., Oke, T.R., 1998b. Radiometric temperatures of urban canyon walls obtained from vehicle traverses. Theor. Appl. Climatol. 60 (1–4), 199–217. https://doi.org/10.1007/s007040050044.
Wang, D., et al., 2020. An advanced geometric model to simulate thermal anisotropy time-series for simplified urban neighborhoods (GUTA-T). Remote Sens. Environ. 237 (September 2019) https://doi.org/10.1016/j.rse.2019.111547.
Wang, D., Chen, Y., 2019. A geometric model to simulate urban thermal anisotropy in simplified dense neighborhoods (GUTA-Dense). IEEE Trans. Geosci. Remote Sens. 57 (8), 6226–6239. https://doi.org/10.1109/TGRS.2019.2904871.

Wang, D., Chen, Y., Zhan, W., 2018. A geometric model to simulate thermal anisotropy over a sparse urban surface (GUTA-sparse). Remote Sens.Environ. 209 (19), 263–274. https://doi.org/10.1016/j.rse.2018.02.051.

Wang, W.M., Li, Z.L., Su, H.B., 2007. Comparison of leaf angle distribution functions: effects on extinction coefficient and fraction of sunlit foliage. Agric. For. Meteorol. 143 (1–2), 106–122. https://doi.org/10.1016/j.agrformet.2006.12.003.

Wang, Y., Gastellu-Etchegorry, J.P., 2020. DART: improvement of thermal infrared radiative transfer modelling for simulating top of atmosphere radiance. Remote Sens. Environ. 251 (August), 112082 https://doi.org/10.1016/j.rse.2020.112082.

Wan, Z., Ng, D., Dozier, J., 1994. Spectral emissivity measurements of land-surface materials and related radiative transfer simulations. Adv. Space Res. 14 (3), 91–94. https://doi.org/10.1016/0273-1177(94)90197-X.

WMO, 2016. In: The Global Observing System For Climate Implementation Needs, p. 316 https://doi.org/GCOS-200.

Yang, H., et al., 2020. Measuring the urban land surface temperature variations under Zhengzhou city expansion using landsat-like data. Remote Sens. 12 (5) https://doi.org/10.3390/rs12050801.

Yang, J., et al., 2020. A semi-empirical method for estimating complete surface temperature from radiometric surface temperature, a study in Hong Kong city. Remote Sens. Environ. 237, 111540 https://doi.org/10.1016/j.rse.2019.111540.

Yin, T., Lauret, N., Gastellu-Etchegorry, J.P., 2015. Simulating images of passive sensors with finite field of view by coupling 3-D radiative transfer model and sensor perspective projection. Remote Sens. Environ. 162, 169–185. https://doi.org/10.1016/j.rse.2015.02.020.

Wan, Z., Dozier, J., 1996. A generalized split-window algorithm for retrieving land-surface temperature from space. IEEE Trans. Geosci. Remote Sens. 34 (4), 892–905. https://doi.org/10.1109/36.508406.